Title

Using X-ray free-electron lasers for spectroscopy of molecular catalysts and metalloenzymes

Journal

Nature Reviews Physics, 3(4)

ISSN

2522-5820

Authors

Bergmann, Uwe

Kern, Jan

Schoenlein, Robert W

et al.

Publication Date

2021-04-01

DOI

10.1038/s42254-021-00289-3

Peer reviewed

New Opportunities at X-ray Free-electron Lasers for Spectroscopy of Molecular Catalysts and Metalloenzymes

Uwe Bergmann[1], Jan Kern[2], Robert W. Schoenlein[1,3],
Philippe Wernet[4], Vittal K. Yachandra[2], Junko Yano[2]

[1]Stanford PULSE Institute, SLAC National Accelerator Laboratory, Menlo Park, California, USA
[2]Molecular Biophysics and Integrated Bioimaging Division, Lawrence Berkeley National Laboratory, California, USA
[3]Linac Coherent Light Source, SLAC National Accelerator Laboratory, Menlo Park, California, USA
[4]Department of Physics and Astronomy, Uppsala University, Uppsala, Sweden

bergmann@slac.stanford.edu, jfkern@lbl.gov, rwschoen@slac.stanford.edu,
philippe.wernet@physics.uu.se, vkyachandra@lbl.gov, jyano@lbl.gov

Key points:

- A description of how femtosecond pulses from X-ray free electron lasers have unique characteristics that makes it possible to use X-ray spectroscopy to follow catalytic reactions at the metal centers in chemical and biological systems under functional conditions and in real time.
- A description of X-ray spectroscopy methods that can be used to study various properties of catalysis and its mechanism at XFELs.
- Hard X-ray absorption and emission spectroscopy (> 5 keV) is used to study transitions from and to the 1s shell (K-edge) and valence electron orbitals of transition metals involved in catalysis to study the geometric and electronic structure of the metal centers.
- Soft X-ray spectroscopy (< 1 keV), transitions from and to the 2p shell (L-edge) of transition metals to the valence orbitals, is used to probe the charge and spin distribution and also degree of covalency of bonds, all properties critical for transition metal-based catalysis.

- Non-linear spectroscopic methods, that are well established in optical and magnetic resonance energy domains, are now being developed in the X-ray domain and their uses and potential of these XFEL-based techniques for the future are described.

Abstract

Metalloenzymes and molecular catalysts are remarkable systems that perform a variety of complex chemical reactions in solution with high efficiency and speed. The metal centers in these systems are responsible for the rearrangement of atoms and electrons during the reactions and they enable selective pathways of charge and spin transfer, bond-breaking/making, and the formation of new molecules. Mapping the electronic structural changes at the metal sites during the reactions gives unique mechanistic insight that has been difficult to obtain to date. The recent development of X-ray free-electron lasers (XFELs) enables powerful new probes of electronic structure dynamics to advance our understanding of metalloenzymes. The ultrashort, intense and tunable XFEL pulses enable X-ray spectroscopic studies of metalloenzymes, molecular catalysts and chemical reactions, under functional conditions and in real time. Our focus in this Technical Review is to describe the current state of the art of X-ray spectroscopy studies at XFELs, and highlight some new techniques that are currently under development. The topic is timely, as more XFEL facilities have started operations with yet more in the planning or construction phase. This enhanced capacity and new capabilities, including high-repetition rate, better XFEL pulse control, and advanced instrumentation, will benefit this exciting field of science. For the first time, we will be able to make real-time molecular movies of metalloenzymes and catalysts in solution, while they carry out chemical reactions.

1. Introduction

More than a century ago (1896), Wilhelm Conrad Röntgen discovered X-rays, revolutionizing imaging technology far beyond the world of science[1]. The power of X-rays led to one of the most profound discoveries of the 20th century: the first high-resolution image of DNA, the molecule of life, revealing its double helix molecular structure[2]. While the penetrating power of X-rays benefits medical and large-scale imaging applications, it is the short wavelength and high energy of X-rays that makes possible the characterization of the atomic and electronic structure of matter that

benefits many areas of science. X-ray diffraction techniques provide atomic-scale structural information of periodic systems (crystalline) and X-ray scattering provides atomic to mesoscale structural information of non-periodic systems (solutions, non-crystalline). Various forms of X-ray microscopy can reveal detailed structural information of complex non-periodic systems with better than 10 nm resolution, and can further provide elemental specificity. The numerous X-ray spectroscopy techniques provide detailed insights into the local atomic and electronic structure, as well as bonding energetics of many systems in an element specific manner (local chemical environment). Ongoing efforts over the past forty years have pushed these methods to ever better resolution and sensitivity with the development of increasingly brighter synchrotron radiation (SR) sources. Here, relativistic electrons circulate in a storage ring, consisting of a series of bend and straight sections. The sideways acceleration of the electrons at the bending magnets creates an intense horizontal fan of SR, and periodic arrays of magnets (undulators, wigglers) in the straight sections force the electrons into slalom-like motions, creating even brighter SR. Several dozen of these facilities now operate worldwide, serving tens of thousands of scientists annually (see e.g. www.lightsources.org). As the latest round of SR facility upgrades is underway, these powerful X-ray light sources are now approaching a physical limit of possible brightness, the diffraction limit. Another limit of SR sources is the duration of each X-ray pulse, typically ranging from 10-100 ps, which defines the fastest time scales accessible with SR (e.g. by stroboscopic probing of dynamics) analogous to the shutter time of an ultrafast camera.

Advancing beyond these limits was enabled by switching from a storage ring to a linear accelerator as the source of relativistic electrons. The reduced electron beam emittance and higher energy, combined with electron bunch compression and a very long undulator (~100 m), caused the electrons to emit radiation no longer individually, but cooperatively in the form of self-amplified spontaneous emission (SASE). The X-ray free electron laser (XFEL) was born. The dramatically increased peak power of XFEL pulses (more than nine orders of magnitude over SR pulses) and the ability to produce extremely short pulses (typically 1-100 femtoseconds (fs) and recently down to the attosecond regime) have revolutionized X-ray science. Femtoseconds (10^{-15} s) are the fundamental time scale for nuclear motion and combining this time scale with the atomic and electronic structure sensitivity of X-rays provides for the first time, simultaneous spatial and temporal access to molecular systems during their various functions as molecules are transformed. How this groundbreaking task can be achieved in metalloenzymes and molecular transition-metal

catalysts, using XFEL-based X-ray spectroscopy in combination with X-ray diffraction and scattering, is the subject of this review.

The ability of transition metals (TMs) to accept and donate electrons, at relatively low energy cost, puts them at the center of many metalloenzymes and molecular catalysts. Among the 3*d* TMs, those with unfilled 3*d* orbitals are of particular importance, as they are the most abundant in nature. (of 3*d* metals Fe, Mn, Ni, Zn, Cu, Co that are most commonly used in catalysis only Zn has a full 3*d* shell and is usually not involved in redox processes). Understanding the chemical function of 3*d* metals, boils down to understanding their 3*d* electronic structure and bonding. X-ray spectroscopy is a powerful probe of the 3*d* metal electronic structure as it probes, directly or indirectly, the binding energetics and the charge and spin states with element specificity. Given the substantial differences in the experimental approaches, we will make a distinction between soft X-ray (<1 keV) and hard X-ray (>5 keV) spectroscopy.

The large difference in absorption cross section and fluorescence yield between soft and hard X-ray spectroscopy has also important practical consequences for the application of both approaches. Here we will focus on photon-in photon-out spectroscopy methods for both hard and soft X-rays, as they are generally applicable and most commonly used for probing chemical reactions of metalloenzymes and molecular catalysts in solution (we note that soft X-ray spectroscopy is also performed in electron and ion yield modes).

Importantly, moving from a synchrotron to an XFEL required a rethinking of experimental approaches with new challenges and opportunities. As described recently by Rossbach, Schneider and Wurth, many of the pioneering experiments at the VUV/soft X-ray FEL FLASH that started user operation in 2005 addressed this issue and thereby laid the foundation for the methods discussed here[3]. An important issue that was identified and persists to date is that of X-ray induced sample damage and a critical question that has to be addressed for each experiment: How can we obtain useful information about the sample without the influence of damage? The standard approach at a synchrotron (where damage typically arises from average X-ray exposure[4]) is to cryogenically cool the sample to reduce the mobility of radicals created by ionization from X-rays. However, this precludes studies under functional conditions. Moreover, while the cryogenic technique with frozen samples works for hard X-rays, it is not suitable for soft X-ray spectroscopy

studies on metalloenzymes. Even with cryo-cooling the radiation damage is too fast for soft X-rays due to the higher absorption cross-section and the larger Auger electron yield. SR studies of metalloenzymes at room temperature are almost impossible at soft X-ray energy range, although recent advances in sample delivery approaches allow some serial measurements at SR sources in the hard X-ray regime (see e.g. [5-9]). Counterintuitively, the peak power of XFEL pulses provide a critical advantage over synchrotrons that opened the door to studies of metalloenzyme samples at room temperature with both hard and soft X-rays. The fs XFEL pulses are so short (~10-50 fs), that one can essentially outrun the sample damage caused by the diffusion of solvated electrons or radicals, by probing the sample and getting useful information, before the onset of damage. This concept of 'probe-before-damage' or 'probe-before-destroy' was first discussed by Neutze *et al.*, who estimated the limits above which damage-induced changes in a biological sample would compromise diffraction data[10]. Subsequently, it was first shown to work experimentally for diffraction by Chapman *et al.*[11], for X-ray emission spectroscopy (XES) of solutions of manganese complexes by Alonso-Mori *et al.*[12] and for soft X-ray spectroscopy of metalloenzymes by Kubin *et al.*[13]. It is now the standard approach for studying many samples at XFELs and for characterizing metalloenzymes and sensitive chemical materials including molecular catalysts *under ambient and functional conditions in real time*.

The work described in this review directly relies on this critically important 'probe-before-destroy' approach. Still, for the successful execution several additional experimental challenges have to be addressed. First, because XFEL pulses often do destroy the sample, its replacement after each pulse by tailored methods of sample delivery and environment are required[14-18]. Second, the stochastic nature of the SASE XFEL pulses causes complex spectral and temporal pulse profiles and significant shot-to-shot spectral, temporal and intensity fluctuations, requiring specialized diagnostics and spectroscopy instrumentation[19-22]. Third, we can study the functional changes in metal centers in real time of the reaction with a pump-probe approach, where a visible laser pump pulse or a trigger such as temperature or a chemical/substrate initiates the reaction, and an XFEL pulse probes the atomic and electronic structure as a function of pump-probe delay time. This method requires shot-to-shot spatial and temporal pump-probe synchronization, spectral and spatial beam diagnostics, detection and data processing. Fourth, the interaction of intense XFEL pulses with matter may create new physical phenomena that need to be understood to properly

interpret the data. We will discuss examples of such nonlinear phenomena and their potential future applications in the last section.

In this review we describe how addressing these four challenges will create new opportunities at the current and next generation of XFELs for spectroscopy of metalloenzymes and molecular catalysts. While presently there are only few XFELs in operation, there is a steady worldwide growth of capacity. With new high-repetition-rate XFELs, such as European XFEL and LCLS-II (Table 1), this capacity increase and the enhanced capabilities of XFELs will be further accelerated. We are optimistic that the explosive growth we saw in synchrotron-based research over the last several decades is an indicator of what we can expect from XFEL-based research in the future, and X-ray spectroscopy of metalloenzymes and molecular catalysts will be a key research area and at the heart of this progress. We also want to point the readers to several recent special issues of journals that provide a broad collection of specialized reviews on this topic[23-26].

2. XFEL Sources, Properties, and New Capabilities

2.1 XFEL Sources and Properties

While optical lasers rely on the quantum process of stimulated emission in a gain medium, typically through multiple passes within a cavity, XFELs amplify coherent electromagnetic radiation using a single pass of relativistic GeV-scale electrons propagating through a very long undulator [27,28] (Figure 1a). This self-amplified spontaneous emission (SASE) mode generates femtosecond coherent X-ray pulses, at multi-gigawatt peak powers, and wavelengths spanning from tens of nm to below 1 Å (photon energies of hundreds of eV to above 10 keV). Thus, the peak brightness of XFEL pulses is ~10^9 times higher than that of current synchrotron X-ray pulses. The XFEL facilities FERMI[29], LCLS[19], SACLA[30], PAL-XFEL[31] and SwissFEL[32] (Table 1) use normal conducting pulsed-radio frequency (RF) accelerator technology operating at repetition rates in the 10-120 Hz range. FLASH[33] and European XFEL[34] facilities use pulsed superconducting accelerator technology creating a burst-mode of pulse trains at 10 Hz, with each macro pulse comprising up to 800 (FLASH) or 2,700 (EuXFEL) pulses. The new XFELs now under development (LCLS-II[35] and LCLS-II-HE[36] in the U.S., and SHINE in China) use

continuous-wave superconducting RF accelerator technology providing high repetition rates with uniform or programmable time distributions. The first of these facilities (project name LCLS-II) is scheduled to start operations in 2022 delivering soft and tender X-ray pulses up to 5 keV (2.5 Å) at repetition rates up to 1 MHz[35]. In the second phase, the X-ray range will be extended beyond 12 keV (1.0 Å)[36]. Other performance enhancements identified by the rapidly growing XFEL user community and demonstrated to date include ultrashort (<1 fs) X-ray pulse generation and characterization[37,38], temporal coherence (near the Fourier-transform limit) via seeding and related schemes[39-46], and versatile operating modes such as two-color multi-pulse sequences[41,44,47-52], and large coherent bandwidth[53]. These enhancements and the fact that the capacity and access to XFELs and lab-based femtosecond sources is growing worldwide[54], will strongly benefit the science enabled by the X-ray spectroscopy and scattering techniques we review in this chapter.

2.2 Time-Dependent X-ray Spectroscopy and Scattering Using an XFEL

Using ultrabright femtosecond XFEL pulses for X-ray spectroscopy (XAS, XES and RIXS methods as described in the Box) has created an enormous potential for time-dependent, *operando* studies of ultrafast dynamics and chemical reactions of metal complexes. The most common approach uses an optical laser pump pulse to initiate the chemical process and an XFEL pulse to probe it. The measurement is repeated at varying time delays between pump and probe to create a sequence of spectra or scattering patterns that reflect the temporal evolution of the system after excitation. Such sequences, sometimes called 'molecular movies', provide a way to follow reactions as they proceed. Critical to the success of this approach is the property of femtosecond XFEL pulses (described in the introduction) to probe the system before destroying it. Femtosecond XFEL pulses are so short, that they can outrun the diffusion of ions, radicals and electrons created by the interaction of X-rays and the sample, which is the main cause of the various forms of radiation damage observed at synchrotron facilities in molecular and biological catalysts [4]. Therefore, cryo-cooling is not required at XFEL experiments[12,55]. The combination of high peak power and ultrashort duration of XFEL pulses, enables us to efficiently probe dilute species of catalysts in solution with sufficient signal to noise. Radiation-sensitive molecular catalysts and metalloenzymes in solution are now routinely studied in XFELs to probe their steady-states[13] and to capture intermediates that occur on slow[56,57] and ultrafast time scales[58-60]. However, at sufficiently high peak power, highly focused XFEL pulses start to create nonlinear effects that

change the X-ray spectra[61-65]. It should be emphasized that these non-linear phenomena and the magnitude of these effects on linear X-ray spectra critically depend on the experimental conditions, such as X-ray wavelength, pulse duration and sample concentration.

For soft X-rays with typical absorption cross-sections of ~10^{-17} to10^{-18} cm^2 and incident fluence of >10^{17} ph/cm^2 within a core-hole lifetime (~4 fs for low-Z elements[66,67]) leads to an appreciable probability of instantaneous nonlinear effects. This corresponds to peak power densities >10^{15} W/cm^2 at 500 eV. Recently a hard X-ray study by Alonso-Mori et al discussed the effects of high-peak power and sample concentration on the X-ray emission spectra of Fe samples of varying concentrations[65]. XFELs based on superconducting linacs such as the existing European XFEL and the future LCLS-II with kHz to MHz repetition rates and the same or smaller pulse energies as existing low-repetition rate XFELs are ideally suited for the traditional X-ray spectroscopy data collection. In some cases, however, nonlinear X-ray phenomena can be exploited to reveal information that is unavailable from linear X-ray spectroscopy and this is an area of active research (see Section 5).

Finally, the XFEL-based pump-probe approach has led to some important experimental changes in hard X-ray spectroscopy as compared to their longstanding use at synchrotron sources. To analyze the emitted or resonantly scattered (photon-out) spectrum at an XFEL, dispersive X-ray optics, where the whole spectrum is recorded in a shot-by-shot approach, are most commonly employed (Box 1)[12]. In hard X-ray spectroscopy, non-resonant XES above the metal K-edge has proven very valuable to early XFEL applications[58,68]. The technique does not require monochromatic X-rays, which has the advantage that it can use the full SASE XFEL pulse, and it can be simultaneously applied with X-ray scattering and diffraction (see Section 3.3), two techniques that provide complimentary atomic structure information[55,57,69].

3. Hard X-ray Spectroscopy at XFELs

Hard X-ray spectroscopy techniques have been widely used for studying molecular catalysts and metalloenzymes at SR facilities. To avoid X-ray induced changes, data are mostly collected at

cryogenic temperature. In this case, only the chemical states that can be trapped by a freeze-quench method are accessible. There have also been various efforts in recent years to collect data at room temperature using jet and microfluidics systems[5-9,70] and these often benefited from sample delivery approaches initially developed for XFEL experiments. At XFELs, the ability to collect X-ray data at room temperature that is free from X-ray-induced changes has made a crucial advancement for mechanistic studies of catalysis, by providing a way to follow reactions as it proceeds after initiating. Among several reaction triggers, so far photochemical pump-probe methods are most often carried out at XFELs, and have provided a way to capture chemical and structural changes at various time delays as short as tens of femtoseconds. The vast majority of catalytic reactions, however, proceed by substrate binding at catalytic sites. Such reactions proceed much slower, due to diffusion-limited processes of substrates. Here the advantage of the probe-before-destroy nature of ultrashort XFEL pulses allows capturing the population shift of reaction intermediates, thus enabling the untangling of the sequence of events at reaction conditions without the requirement of cry-cooling.

While soft X-ray L-edge spectroscopy (Section 4) is a more direct probe of the 3*d* TM metal electronic structure, the hard X-ray regime offers several practical advantages, as experiments under ambient pressure conditions and on bulk materials are facilitated due to their larger penetration depth. Furthermore, the shorter hard X-ray wavelengths (~1-2 Å) are comparable to atomic distances, allowing simultaneous scattering/diffraction experiments that provide structural information at atomic resolution. In this section we describe examples of time-resolved XES and XAS experiments (Sections 3.1 and 3.2, Figure 2), and multimodal experiments using combinations of spectroscopy and diffraction measurements with hard X-rays (Section 3.3, Figure 3).

3.1 X-ray Emission Spectroscopy (XES)

XES probes occupied states and can be performed off resonance with any incident photon energy and bandwidth that is above the absorption edge region of the absorbing metal (Box 1), allowing the use of the full XFEL SASE pulse and combining the technique with scattering/diffraction. XFEL-based XES has been used widely to study changes in metal oxidation and spin states of enzyme systems including the heme-Fe in cytochrome c[58,59] (Figure 1c) and in myoglobin[60], the

Mn_4Ca cluster in photosystem II[17,55-57,71] (Section 3.3) the dinuclear Mn-Fe site in ribonucleotide reductase (RNR)[17] (Figures 2b, 3b) and the dinuclear Fe-Fe site in methane monooxygenase[72]. Numerous other photosensitive TM complexes have been studied to understand the initial steps of photo excitation and light induced charge transfer and the time resolved XES provided detailed information about changes in the effective spin of the TM[68,69,73-78] (e.g. Figure 2c).

While most XFEL-based XES studies have focused on the stronger $K\alpha_{1,2}$ and $K\beta_{1,3}$ XES lines, the weakest XES lines resulting from dipole-allowed valence-to-core transitions (VtC, also known as $K\beta_{2,5}$ and Kβ'', see Box), contain the most detailed information about the bonding and chemical environment of the absorbing atom[79,80]. Recently steady state[81] and time-resolved VtC XES using an XFEL was reported[82] (Figure 2d). Comparing the observed spectral changes for three Fe(CN)-bipyridine compounds, recorded 0.2-50 ps after light excitation, with density functional theory (DFT) calculations revealed the sensitivity of VtC XES to bond length expansion. It was found that the integrated intensity of the VtC XES spectrum is a measure of the metal-ligand bond length because it is primarily determined by the overlap of ligand valence orbitals with metal n*p* orbitals. A decrease of intensity with increasing metal-ligand distance was observed. The spectra also showed signatures of photooxidation as measured by the energy position of the VtC XES spectrum where a blueshift was associated with increased oxidation state of the Fe center. With further evidence of ligand dissociation for $Fe(CN)_6$, and metal centered triplet and quintet states for $Fe(CN)_4(bpy)$ and $Fe(CN)_2(bpy)_2$, respectively, the study concluded that the metal-ligand bond length expanded by either 0.1 or 0.2 Å upon formation of the respective metal centered triplet or quintet state in the sub-ps time scale[82] (Figure 2d).

3.2 X-ray Absorption Spectroscopy (XAS)

The XANES region of XAS probes the unoccupied states via metal 1*s*→n*p* transitions (Box) and, like XES, XAS can reveal details of ultrafast changes in the environment of TMs in natural and synthetic molecules. Unlike XES, however, XAS measures changes of absorption coefficient around the metal absorption edges and therefore requires monochromatized incoming X-rays to scan through a wide energy range (< 50 eV for XANES and > 500 eV for EXAFS, Box 1). To observe small spectral changes, the normalization of data at each incoming X-ray energy,

considering the fluctuation of both incoming X-ray energy and probing sample volume during the shot-by-shot experiments at XFELs is crucial. Energy dispersive XAS using a wide energy range has also been described[83]. It should be noted that when using monochromatized beams the flux is reduced by about a factor of 100 although this reduction can be less if using seeded beams.

Lemke *et al.* used XAS at an XFEL to observe the formation of a high spin state ~160 fs after light excitation in a Fe-trisbipyridine compound, and indications of a metal-ligand charge transfer (MLCT) state at very short times[84]. Fe K-edge XAS was also used to study the ultrafast photodissociation process of CO bound to the heme group in myoglobin[85]. Changes of the Fe K-edge energy and intensity were fit by two processes with characteristic times of 70 and 400 fs. The faster process was interpreted as being connected to an elongation of the Fe–N bond length in the heme, coupled to a shortening of the Fe–His bond. The slower process was interpreted as an iron out-of-plane motion coupled to the motion of the helix F of the myoglobin, being the first step in the observed protein quake and these spectroscopic results agree well with independently conducted time resolved crystallographic experiments in the sub-ps time scale[86]. Interestingly, a recent XES study on photodissociation of NO-bound myoglobin showed that within 100 fs a ligand free triplet state is formed and that it takes about 800 fs to form a domed high spin quintet state[60]. The sensitivity of XAS to structure and ligand environment is due to that metal 1*s*→n*p* transition energies and intensities change when metal-ligand orbital overlap and ligand-fields change[87]. Examples for other ultrafast XAS studies include measurements on Cu-phenanthroline[88] or on Ni porphyrins[89]. It is possible to extend the information content that can be obtained by XAS studies when using polarized photoexcitation. The idea is to use the fact that optical excitation in metal complexes is often anisotropic and by setting different relative polarizations of optical pump and X-ray probe beams one selects different sub-ensembles of differently excited species. Polarized cobalt XAS studies on a cobalamin derivate (Figure 2e) for example showed that structural changes upon photoexcitation of the corrin ring occur mainly in the ring plane first along one direction at 19 fs, then in the perpendicular direction of the ring 50 fs later, followed by elongation of the axial ligands on a 200-250 fs time scale and internal conversion to the ground state occurs on a 6.2 ps time scale. These results describe the features that influence the reactivity, stability and deactivation of electronically excited cobalamins[90,91] (Figure 2e).

To obtain very precise measurements of distance changes of the ligands of TM systems, EXAFS is an essential tool in SR studies. Recently, the EXAFS region of XAS was successfully collected at XFELs[92,93]. Precise signal normalization to the incoming beam intensity and the probed sample volume is critical when measuring the subtle changes in EXAFS spectra. This was achieved by recording the forward scattering signal from the solvent for each shot and using it for signal normalization. Time-resolved EXAFS with delay times of 0 to 600 fs and 10 ps on a solution of $Fe(terpy)_2$ showed a 0.2 Å change in the Fe-ligand distance between the ground state and the excited state and revealed an intermediate spin state in the laser induced low-spin (LS) to high-spin (HS) transition in the 100 fs time scale[93] (Figure 2f). In the HS final excited state all Fe-N bonds were found to be expanded by ~0.2 Å. The intermediate state was best explained by expansion of the equatorial Fe-N bonds by 0.15 Å, while the axial Fe-N bonds did not yet expand[93].

3.3 Multimodal Measurements

Combining complementary techniques leads to a more complete picture of the local changes of a TM site during a reaction. An example is the use of both XAS and XES to study the weak covalent bond between the heme Fe and an S-Methionine (Met) ligand present in cytochrome c (Figure 1d)[58]. The presence of this bond ensures that the Fe stays in its low-spin (LS) state in both Fe^{II} and Fe^{III} oxidation states. Loss of the S-Met bond changes the functionality of cytochrome c. The bond can be broken by laser excitation after which it quickly reforms. 600 fs after excitation changes in the XAS spectrum indicate a change from a six-coordinate LS to a five-coordinate HS Fe configuration, including loss of the S(Met) ligand and elongation of the His-Fe bond length (Fig. 2f). The sensitivity to structure and ligand environment with XAS was complemented with Kβ XES (Figure 1c, middle) that gives access to the metal spin state (number of unpaired electrons in the metal-derived 3*d* orbitals). This provided a 6.1 ps time constant for re-formation of the LS state, and a 6.4 ps time constant for heat transfer out of the heme. The study shows that the Fe – S(Met) bond enthalpy is stronger in the presence of protein constraints, demonstrating how biological systems use subtle differences in energetics to control chemical function of TM systems[58]. A recent XES and XAS study on ferric cytochrome c found that heme-doming is also occurring in ferric hemes upon photodissociation of bound ligands and results from populating high spin states[59].

Ideally, one would like to use multimodal techniques, simultaneously, to minimize systematic errors potentially introduced by varying conditions from each separate experiment such as varying sample conditions or varying time zero of optical pump and X-ray probe. The combination of XES from two different metals[17,94-96], or XES with scattering/diffraction is well suited for this approach, as the incident X-ray energy can be freely selected (as long as it is above the absorption edge). We provide examples of these approaches below.

Canton *et al.*[97] combined XES with X-ray diffuse scattering (XDS) to monitor the ultrafast electron transfer in a Ru-Co dyad following excitation with a fs pump laser (Figure 3a). The dyad employed is a representative model for many synthetic and natural photocatalysts with a distance between electron donor (Ru) and acceptor (Co) of about 13 Å. While Co Kα XES was used to follow the changes in oxidation state of the Co center and hence the kinetics of electron transfer, the XDS signal was used to follow structural changes in the dyad. The Kα XES, in addition to transient optical absorption spectra (TOAS), revealed that the electron transfer occurs in a two-step mechanism with initial formation of a LS Co(II) species (500 fs) and subsequent conversion to a HS Co(II) within 2 ps. The simultaneously recorded X-ray scattering also revealed a fast change in the Co binding environment by 0.2 Å and showed that charge separation is faster (~2 ps) than the thermalization of the excitation energy with the surrounding, that was observed at around 12 ps[97].

Another example for measurements of XES and X-ray diffraction (XRD) is the work by Fuller and colleagues on Mn/Fe containing ribonucleotide reductase (RNR)[17]. Here XES of both Mn and Fe, as well as X-ray diffraction was measured, simultaneously, on crystals of RNR in the aerobic $Mn^{III}Fe^{III}$ state confirming the oxidation state of the metal centers as well as showing the undamaged structure of the active site at room temperature (Figure 3b).

The prime example for simultaneous use of XES and XRD is the series of studies on Photosystem II (PS II) crystals [55-57,98]. PS II is a metalloenzyme that catalyzes the light driven oxidation of water to molecular oxygen in a four-step reaction cycle (Figure 3c) and has been widely studied using XFELs[55-57,98-103]. The catalytic site contains a Mn_4CaO_5 cluster embedded in the large protein complex. Each step is driven by the absorption of one photon and the Mn_4CaO_5 cluster acts as a

site of charge accumulation to finally catalyze the oxidation of two molecules of water to release molecular oxygen, four protons and four electrons. Very radiation sensitive samples like PS II are very difficult to study under functional conditions with x-rays[104], but, as discussed above, the ultrashort XFEL pulses can outrun the damage they cause. Combined XRD and XES studies initially confirmed that the Mn_4CaO_5 cluster in PS II is in an intact, non-reduced state in the microcrystals used for the diffraction measurements[55]. Mn Kβ XES for the four stable intermediate states of the Mn cluster[56] indicated proper in-situ turnover of the PS II enzyme under the illumination conditions and allowed to estimate the population of each of the intermediate states in the sample (Figure 3c). The XRD obtained in parallel showed that the Mn cluster undergoes a structural rearrangement in the S_2-S_3 transition that consists of a widening of the cluster and insertion of an additional oxygen bridge between Mn and Ca to form a Mn_4CaO_6 cluster, different from earlier results at lower resolution[101,102] and confirmed by a second independent study[103]. Subsequent time resolved data collection of both XES and XRD[57] revealed the time constant of this transition to be around 300 µs based on the XES data and showed that several amino acid residues in the vicinity of the Mn_4CaO_5 cluster first undergo structural changes, followed by an expansion of the metal cluster and subsequent insertion of the new oxygen bridge. Based on the XES it was possible to conclude that Mn oxidation and insertion of the new oxygen occur concomitantly[57] (Figure 3c).

4. Soft X-ray Spectroscopy at XFELs

Soft X-ray spectroscopy of metalloenzymes and molecular catalysts at XFELs uses the advantage of directly probing the local electronic structure of 3*d* TMs via the dipole-allowed $2p \rightarrow 3d$ transitions at the metal L-edge. Tunability and high intensity of the soft X-ray XFEL radiation are essential to address the dilute metal species in solution. Femtosecond duration of the XFEL pulses is necessary in different ways and this defines the two classes of applications we discuss with Figure 4: i) Probe-before-destroy spectroscopy where high-valent metal sites in inorganic molecular complexes and metalloenzymes are studied with L-edge XAS (Section 4.1., Figure 4a-d). Here, the high-valent metal species are probed with femtosecond pulses before X-ray induced damage of the sample sets in. ii) Time-resolved $2p3d$ RIXS where femtosecond resolution in optical pump and X-ray probe experiments gives access to the frontier-orbital interactions in short-lived reaction intermediates (Section 4.2., Figure 4e-j). Here, RIXS is used to probe ligand-field

(LF) and charge-transfer (CT) transitions during molecular transformations and in excited-state dynamics. All examples are photon-in photon-out experiments on liquid samples relying on the bulk sensitivity of the respective methods. Liquid jets are used to prepare the solution samples in the vacuum environment necessary for soft X-rays with fast sample replenishment to avoid X-ray induced sample damage from consecutive X-ray pulses. Many of the early soft X-ray investigations at XFELs aimed at proving that undistorted signals of intact samples could be measured[3] (and references therein, [105]). While we focus on homogeneous transition-metal catalysts, we note that other important applications of soft X-ray spectroscopy at XFELs are in surface science and heterogeneous catalysis[106-110], in photochemistry of small molecules and organic systems in solution[111,112] and in the gas phase[113-115].

4.1. X-ray Absorption Spectroscopy (XAS)

The Mn L-edge XAS study by Kubin *et al.* in Figure 4a exemplifies the use of XFELs for probe-before-destroy spectroscopy at room temperature of solutions of high-valent Mn species in inorganic complexes and in PS II[13]. The motivation is to study high-valent metal sites in inorganic molecular complexes and metalloenzymes at functional conditions (room temperature solution) in order to relate their reactivity to the probed electronic structure. Successful implementation of such experiments requires i) specialized liquid-jet sample delivery, ii) intense femtosecond X-ray pulses, and iii) efficient soft X-ray spectrometers for partial-fluorescence yield XAS. Low-consumption liquid jets are needed to prepare the often precious and dilute solutions with typical metal concentrations in the mM range[15]. The femtosecond pulse length is essential to avoid photoreduction and probe the sample before ions, radicals and electrons created by the ionizing soft X-ray radiation in the solvent, ligands or protein environment reduce the high-valent metal centers. As the level diagram in Figure 4b shows, incident X-rays tuned to metal L-edge also ionize non-resonantly light elements (C, N, O) in the sample (solvent, protein, ligands) followed by emission of their characteristic X-ray fluorescence. Efficient soft X-ray spectrometers are necessary to discriminate the metal fluorescence of interest from this light-element fluorescence background.

High throughput is essential to address the low (mM) concentrations of metals in inorganic catalysts and metalloenzymes. The successful implementation of the example in Figure 4a at the LCLS XFEL shows that these requirements can all be met. The spectra of the high-valent Mn^{III} and Mn^{IV} complexes in Figure 4a do not contain significant amounts of the most reduced Mn^{II} state as present in the mixed-valent Mn^{II}-Mn^{III} compound (peak around 639.5eV). The spectra shift to higher energies with increasing Mn oxidation state with a blue-shift of 1.5-2 eV per unit increase of oxidation state as shown in Figure 4c. This plot now also includes the Mn L-edge measurements of two states of the water oxidation catalyst Mn_4CaO_5 in photosystem II solution and the measured photosystem II spectra consistently shift with oxidation state. This establishes probe-before-destroy soft X-ray spectroscopy at XFELs and opens the door to a new way of probing the electronic structure in inorganic catalysts and metalloenzymes at functional conditions in room-temperature solutions with soft X-ray L-edge spectroscopy.

Future prospects of this approach include gaining more detailed insight into how the metal L-edge XAS spectrum probes charge and spin densities at high-valent metal sites. Quantum-chemical calculations indicate that the local charge at the metal site does not change considerably with changing oxidation state[116,117] and the examples Figure 4d illustrate this. For the reduction of both the simple $Mn^{III}(acac)_3$ complex and the much larger iron heme a complex, the displayed calculations show that the added charge density effectively spreads over the whole molecule while the added spin density accumulates locally at the metal center. Relating such calculations of charge and spin density distributions with measured L-edge XAS spectra as done in ref. [116] for $Mn^{III}(acac)_3$ (see Figure 4a for the spectrum of $Mn^{III}(acac)_3$) has already led to a new understanding of metal L-edge XAS. With future developments in ab initio theoretical descriptions of the electronic structure and X-ray spectra[118], in particular, the ability to describe multinuclear metal centers, a detailed understanding of charge and spin density changes in the redox reactions of inorganic compounds and metalloenzymes will be accessible with soft X-ray L-edge spectroscopy at XFELs.

4.2. Resonant Inelastic X-ray Scattering (2*p*3*d* RIXS)

The essence of the optical pump and X-ray probe experiment in Figure 4e-g is very simple[119]: A metal to ligand charge transfer (MLCT) excitation induces dissociation of a ligand form $Fe(CO)_5$ in solution and creates the reactive intermediate $Fe(CO)_4$ (Figure 4g). As the Fe-CO bond breaks

and new bonds are formed in the course of the reaction, covalent metal-ligand interactions change. This process was probed with time-resolved Fe 2*p*3*d* RIXS (for the *ab initio* calculations of X-ray spectra used to assign species and for more details see [87,119-121]. The measured RIXS intensities in Figure 4e are plotted as a function of incident energy ($h\nu_{in}$) versus energy transfer ($\Delta E = h\nu_{in} - h\nu_{out}$). The encircled maxima are most informative and they are due to Fe 2*p*→LUMO(dσ*) transitions with inelastic scattering to final states, where ΔE corresponds to HOMO-LUMO(dπ→dσ*) excitations (Figure 4g). ΔE decreases from $Fe(CO)_5$ to $Fe(CO)_4$ as covalent metal-ligand interactions and the HOMO-LUMO energy difference decrease (**1** in Figure 4e, $Fe(CO)_4$ is the most abundant species at pump-probe delays of 0-700 fs). Consistently, as the LUMO energy decreases, the Fe 2*p*→LUMO(*dσ**) resonance red shifts. 2*p*3*d* RIXS therefore probes bonding at the Fe center via the HOMO-LUMO(*dπ→dσ**) LF transitions. They are selectively probed and resonantly enhanced by tuning the incident photon energy to the Fe 2*p*→LUMO(*dσ**) resonance. A parallel pathway was also observed in which an ethanol solvent molecule attaches to the Fe center in $Fe(CO)_4$ to form an $Fe(CO)_4$-EtOH solvent complex. This is seen in the RIXS measurement with intensities marked **2** in Figure 4e: HOMO-LUMO excitation energies are increased compared to **1** because forming the bond in $Fe(CO)_4$-EtOH partially restores the covalent Fe-ligand interactions and pushes apart HOMO and LUMO (Figure 4g, the 2*p*→LUMO resonance energy is increased consistently as the LUMO energy is increased). In the discussion here, the different spin states of $Fe(CO)_4$(singlet excited-state and triplet, Figure 4g) are not distinguished in that they both contribute to the circled region **1**. However, they can be distinguished by when they arise in the reaction, and the integrated RIXS intensities plotted versus time delay (Figure 4f) are a measure of how the populations of singlet excited-state and triplet $Fe(CO)_4$ (**1**) and the $Fe(CO)_4$-EtOH solvent complex (**2**) change over time. The combination of femtosecond 2*p*3*d* RIXS with ab initio calculations revealed that the reactivity of the transient intermediate $Fe(CO)_4$ in terms of binding molecules is determined by the population of the LUMO(dσ*) orbital[119]. When it is populated, as in singlet excited-state and triplet $Fe(CO)_4$, ligand-to-Fe σ donation is impeded and these species are unreactive (do not bind any molecule) on the probed time scales. $Fe(CO)_4$-EtOH in turn is formed by binding ethanol to singlet ground-state $Fe(CO)_4$, which has an empty LUMO orbital and is formed by electronic relaxation. It will be interesting to see in future applications of 2*p*3*d* RIXS at XFELs how this approach can be used to understand and ultimately control the reactivity of new photocatalytic systems in solution.

Building on seminal L-edge XAS work[122], the studies on iron hexacyanide $Fe(CN)_6$ in solution in Figure 4h-j exemplify how time-resolved 2*p*3*d* RIXS at XFELs can be used to map transient charge distributions[105,123]. In contrast to the former example, the molecule now stays intact but valence-orbital occupations change. The 2*p*3*d* RIXS intensities for ferric (Fe^{III}) and ferrous (Fe^{II}) cyanide (Figure 4h) demonstrate how RIXS reflects valence-orbital occupations in the ground states of the two compounds (valence configurations of the Fe-centered orbitals are $t_{2g}^5 e_g^0$ for Fe^{III}-cyanide and $t_{2g}^6 e_g^0$ for Fe^{II}-cyanide, both with octahedral, O_h, symmetry). The hole in the t_{2g} orbital in ferric Fe^{III}-cyanide (Figure 4j) gives rise to a $2p \rightarrow t_{2g}$ resonance that is missing in ferrous Fe^{II}-cyanide, while both compounds exhibit $2p \rightarrow e_g$ and $2p \rightarrow \pi^*$ resonances. 2*p*3*d* RIXS in this example probes the $t_{2g} \rightarrow e_g$ LF transitions (**1** in Figure h, j) and the $t_{2g} \rightarrow \pi^*$ CT transitions (**2** in Figure h, j). By tuning the incident photon energy, the LF (**1**) or CT transitions (**2**) can be resonantly enhanced (evidently, ligand σ/π to t_{2g} excitations only appear in Fe^{III}-cyanide, * in Figure 4h, j). Figure 4i now shows how the Fe 2*p*3*d* RIXS intensities change when going from the ground state to the ligand to metal charge transfer (LMCT) excited state of Fe^{III}-cyanide as generated by optical excitation. Femtosecond resolution was needed here to catch the transient intermediate LMCT state. As can be seen in the calculated charge densities in Figure 4j, where charge decrease on two ligands and charge increase at the Fe center, LMCT excitation of Fe^{III}-cyanide promotes an electron from a ligand σ orbital to the Fe-centered t_{2g} orbital resulting in the LMCT excited-state configuration $*Fe^{III}$ $t_{2g}^6 e_g^0$. In the time-resolved RIXS measurement the signatures of ground-state Fe^{III}-cyanide decrease (blue in Figure 4i, the $2p \rightarrow t_{2g}$ resonance disappears in particular, as the t_{2g} shell is filled) and the new intensities (red) characterize the LMCT $*Fe^{III}$ excited state. Since both, Fe^{II}-cyanide and LMCT $*Fe^{III}$-cyanide, have the same $t_{2g}^6 e_g^0$ configuration, these intensities measure the transient effect of the ligand σ hole (Figure 4j). In LMCT $*Fe^{III}$-cyanide the $2p \rightarrow e_g$ resonance (**1**) is red-shifted by 1 eV compared to Fe^{II}-cyanide and this indicates that the 2*p* core hole is better screened in the XAS final states of LMCT $*Fe^{III}$-cyanide. This stabilization of the 2*p* core-excited states indicates that the charge density locally at the Fe is higher in LMCT $*Fe^{III}$-cyanide compared to Fe^{II}-cyanide. Indeed, calculations confirm that the ligand σ hole in LMCT $*Fe^{III}$-cyanide induces an increase of charge density at Fe[123]. Calculations also detail that this charge increase is due to an increase of ligand-to-Fe σ donation. This strengthens the Fe-ligand bond and increases the ligand field strength 10Dq[123,124]. 2*p*3*d* RIXS measures this by an increase

of the $t_{2g} \rightarrow e_g$ transition energy of 0.3 eV in LMCT *Fe^{III}-cyanide compared to Fe^{II}-cyanide (**1**, Figure 4i and h). Such detailed insight into transient charge distributions made accessible by time-resolved 2*p*3*d* RIXS could prove essential in the development of efficient photocatalysts by probing, e.g., the effects of manipulating ligands in metal complexes to control excited-state dynamics [125] or by resolving the charge-transfer dynamics between metal complexes and solid-state surfaces in dye-sensitized semiconductor devices.

The element-, site- and orbital-specific access to photochemical reaction mechanisms as demonstrated here enables correlating orbital symmetry and interactions, spin multiplicity and reactivity of metal compounds in solution. In future applications, this ability promises unique insight into the photochemical reaction dynamics of fundamentally important metal complexes, functional photocatalysts and dilute bioinorganic systems. High-repetition rate XFELs such as the European XFEL and the high-repetition rate LCLS-II will enable systematic soft X-ray spectroscopy of functional systems in solution at the mM concentration level at metal L-edges with XAS and 2*p*3*d* RIXS.

5. New Capabilities and Methods at Future XFELs

In sections 3 and 4 we have focused on linear X-ray spectroscopy methods, in which the material response (or signal of interest) is independent of the X-ray intensity. Nonlinear X-ray spectroscopy accesses new aspects of matter where the response depends on the X-ray intensity. These fundamentally new forms of X-ray spectroscopy build upon the rich developments in nonlinear optics, and offer qualitative new scientific insight through element specificity, atomic spatial resolution, and sub-femtosecond time resolution. In the following we highlight a few emerging nonlinear X-ray spectroscopy methods that are particularly promising for a deeper understanding molecular catalysts and metalloenzymes. Note that this section is not comprehensive of the rich area of nonlinear X-ray science that has been opened by XFELs, which includes important advances in nonlinear scattering[126-128] two-photon absorption[129], second harmonic generation[130], and transient grating methods[131-133] to name a few.

5.1 Stimulated XES - Extracting VtC, Kβ, Soft XES, and Other Weak Emission Lines

Spontaneous XES is a powerful element-specific probe, but is subject to relatively weak emission cross-sections, and photons are emitted in all directions. Stimulating the emission offers three potential advantages: (1) signals are emitted along a well-defined X-ray beam direction enabling efficient collection of the entire signal, (2) strong signal enhancements that can out-compete other decay channels, (3) spectral narrowing and selective stimulation may result in enhanced chemical sensitivity.

Strongly enhanced stimulated Kα emission and RIXS has been observed in Ne gas[134,135] and in 3*d* transition metal systems[136,137]. The two main approaches are amplified spontaneous emission (ASE)[134,136,137] and seeded stimulated emission[135,136], as illustrated in Figure 5a. In ASE, an intense X-ray pump creates a population inversion along the propagation path. Spontaneously emitted photons along the population inversion path can stimulate the emission of additional photons at the same wavelength and direction, resulting in an ASE signal that grows exponentially (Figure 5a). Kα ASE can be used for spectroscopy as it exhibits chemical shifts and strong spectral gain narrowing[137]. To stimulate the spectroscopically more sensitive Kβ and valence-to-core (VtC) emission lines, a second-color seed pulse is tuned to their respective energy (Figure 5a). The seeding approach is required as Kα amplification always dominates the weaker Kβ lines.

Seeding of Kβ emission from a $NaMnO_4$ solution with an enhancement of more than 10^5 compared to spontaneous emission into the same solid angle was recently reported[138]. The team also observed strong spectral narrowing (Figure 5a). While the experimental conditions in that work were not optimal for performing spectroscopy, seeded stimulated emission is a potentially very powerful tool for ultrafast chemical analysis. Besides the practical advantages of larger signal and outcompeting other decay channels, we envision employing seeded stimulated emission to enhance individual spectral features characteristic of the electronic structure of a species of interest while potentially suppressing the core-hole lifetime broadening. Tuning to resonant features at the absorption edge, can widen this approach to stimulated RIXS[135]. The enhanced spectral sensitivity and control will widen XFEL based spectroscopy to reveal subtle electronic structure changes that are currently below the detection limit. Such studies will include complex systems and ultrafast intersystem crossings in 3*d* metal centers of light-harvesting and photocatalytic molecules.

5.2 Metal-Ligand Double Core Hole Spectroscopy

An important challenge for photo-catalysis is understanding coupled valence states (e.g. where metal and ligand orbitals mix) that mediate charge separation and reactivity. A powerful element-specific approach relies on the simultaneous creation of two core-level transitions in adjacent atoms, e.g. one from a metal and one from a bonded ligand atom or metal (see schematics in Figure 5). Theoretical studies of the creation of such double-core-hole (DCH) states date back to 1986 when Cederbaum *et al.* predicted that the binding energies associated with DCHs at different atomic sites of small molecules could sensitively probe the chemical environment of the ionized atoms[139]. Since then, most theoretical studies[140-144], synchrotron experiments[145-150] (where the DCH states were created by one photon ejecting two core electrons) and XFEL experiments[151-156] (where two photons create the DCH state) have focused on probing the chemical environment of atoms in small gas phase molecules.

The application of DCH spectroscopy to 3*d* transition metal compounds has been discussed in a recent theoretical study of VtC-XES in mononuclear Mn complexes and binuclear Co complexes with metal-metal direct bonds[157]. For the mononuclear Mn complexes the VtC-XES signals of the metal-1s/ligand-1s DCH states, and for the binuclear Co complexes the VtC XES for the two-site Fe and Co 1s DHC states were calculated and compared to the conventional single core hole (SCH) VtC-XES signals. Figure 5b shows the schematics of DCH VtC-XES and a comparison of DCH and SCH VtC-XES signals of these systems.

The calculations show that in the mononuclear Mn complexes the XES signal of the metal-1*s*/ligand-1*s* DCH states, reveals additional information on the chemical bonds between the metal center and the coordinating atoms. Similarly, the two-site 1*s* DHC states in dinuclear compounds show spectral changes of features including those related to ligand orbitals as compared to the SCH states. The size of these shifts also reveals that in the dinuclear Co complex the metal-ligand interaction is stronger than that in the dinuclear Fe complex. These simulations show that through the perturbation introduced by a second core hole near the studied core hole, DCH VtC-XES can go beyond the conventional SCH VtC-XES techniques and provide further information on the local electronic structure of the core holes and especially the interaction between the two atoms with core holes. DCH VtC-XES has the potential to become a new research tool in transition metal

complex chemistry. In the future, one might be able to extend the DCH approach to RIXS and combine it with stimulated emission discussed in the previous section.

5.3 Wave-Mixing and Multidimensional Spectroscopy

In addition to stimulated emission and double-core-hole methods new nonlinear and multidimensional X-ray spectroscopies will provide important new insight to functioning photocatalysts by mapping coherent charge flow and energy relaxation on fundamental time scales with access to the full range of valence states (unrestricted by dipole selection rules). The element specificity of core-level X-ray resonances can reveal charge and energy flow between constituent atoms in molecular complexes. This insight is not achievable with conventional optical ultrafast probes, and will provide critical insight to molecular catalysts with strong coupling between electronic and nuclear dynamics. High-repetition-rate XFEL sources will be essential to realize the potential of these new approaches by enabling experiments in the perturbative small-signal regime, with pulses of lower peak power, thereby avoiding the complications from higher-order nonlinearities that arise in the strongly nonlinear regime.

One promising example of this class of experiments is X-ray core-hole correlation spectroscopy (XCCS) as illustrated in Figure 5(d-f). This approach probes the degree of mixing of excited molecular orbitals (i.e. correlations between valence excited states) associated with different atomic sites in a molecule[158-160] and is analogous to two-dimensional (2D) electronic spectroscopy[159,161,162] but with the element specificity of X-rays.

Figure 5 presents an example in aminophenol where XCCS probes the orbital mixing (quantum coupling) between nitrogen- and oxygen-associated valence states in different isomers. Here, two pulses probe the aminophenol molecule in resonance with the N-1*s* ($\hbar\omega_N$ ~400 eV) and O-1s ($\hbar\omega_O$ ~535 eV) core excitations, respectively. In a coherent four-wave mixing implementation, the initial excitation is created by a pulse pair, and a third pulse (in a phase-matched geometry) reads out the scattered Raman signal. Thus, XCCS measures a third-order, $\chi^{(3)}$, four-wave mixing process, whereby a sequence of three incident pulses (three fields), $E_n(k_n,\omega_n)|n = 1, 2, 3$, generate a stimulated signal, e.g., $E_{sig}(-\omega_1 + \omega_2 + \omega_3)$, in the momentum-matched direction, $k_{sig} = -k_1 + k_2 + k_3$. A 2D spectral map of the valence electronic structure is created with one axis, ω_S, determined by the spectrum of the emitted signal (measured with a dispersive X-ray spectrometer) and the

other, ω_{12}, determined by the Fourier transform of the signal with respect to the time delays of the first two phase-locked pulses. (Note that sub-fs phase-lock pulse pairs in the X-ray regime have recently been demonstrated at LCLS[38]). The presence of off-diagonal features in this 2D map reflect the degree of orbital mixing between the two excited valence states associated with the N and O atoms; no signal should be seen in the Hartree-Fock limit of independent orbitals. Calculations show that the extent of this orbital mixing depends not only on molecular structure (i.e., it is stronger in ortho-aminophenol with adjacent orbitals, compared to the para conformation), but also on the nature of the molecular orbitals excited within the energy envelopes (~10 eV) of ω_N and ω_O[158,160].

As indicated in Section 2.2, in the soft X-ray range, an incident fluence of ~10^{17} ph/cm^2 can lead to appreciable nonlinear effects. In the case of XCCS, the pulse duration must be comparable to (or less than) the order of the core-hole lifetime (~4 fs for low-Z elements[66,67]) since Auger decay suppresses the correlation signal of interest. This corresponds to ~10^9 photons/pulse in a 1 μm focus (~10^{15} W/cm^2 at 500 eV). Estimates based on X-ray nonlinear susceptibilities lead to similar conclusions for the required X-ray peak power density[160,163]. Note that modern nonlinear optical spectroscopy experiments typically operate in the perturbative regime, ~0.1 photons per cross-section, in order to avoid distortion of the spectral signal of interest from higher-order nonlinear processes, saturation, nonlinear waveguiding, and other undesirable effects. This is important in order to extract readily interpretable new scientific information about the complex under study, and is in contrast with the strongly nonlinear regime where signals may be larger but much more complicated and difficult to interpret.

6. Outlook

The first decade of XFEL science has brought us many striking results and the emergence of exciting new research areas[19,23-25,164,165]. In this review we have discussed novel XFEL-based spectroscopy methods on metalloenzymes and molecular catalysts and their future opportunities. While tremendous progress in every aspect of XFEL research has been made over the last decade, much work is still ahead when it comes to making the best use of this powerful tool. Much of the

research techniques are not yet fully optimized and compared to most synchrotron experiments, most XFEL experiments are complex undertakings that are far from turn-key operations. As the performance parameters of the current and next generation of XFELs have been defined, we believe that addressing three critical areas will help in optimizing future XFEL science on metalloenzymes and molecular catalysts:

1) **Improved instrumentation for XFEL experiments including beam diagnostics, pulse control, X-ray optics, sample synthesis and delivery and data acquisition & control systems.** The large shot-by-shot variations of XFEL pulses require precise diagnostics for data normalization and arrival-time jitter, especially when measuring small spectral changes. XFEL facilities are actively working on improving such diagnostics and enhancing the pulse control to reduce the fluctuations. Making the best use of each XFEL pulse requires to increase further the photon-out signal, including more efficient optics and detectors, as well as better sample quality and delivery. We estimate that there is an order of magnitude that can be gained once everything is optimized.
2) **Development of a more complete theoretical description of the systems under study, the interaction of pump/probe pulses with the sample, and the resulting spectral or diffraction features.** Applications of *ab initio* theories to effectively describe the electronic structure and X-ray spectra of metal complexes and metalloenzymes are rapidly evolving ([118] and references therein). For the purposes discussed here, they seem best suited to relate X-ray spectroscopic observables and mechanistic understanding of reactivity in catalysis. Enhanced computational power and more efficient descriptions will enable the improvement of such theories and simulations that match the improved experiments. Challenges include effective descriptions of femtosecond excited-state molecular dynamics simulations of transition-metal systems, efficient multiconfigurational approaches to the valence and core electronic structure in transition-metal complexes and photocatalysts with numerous 3*d* electrons and open shells, as well as the efficient description of bonding, orbital interactions and X-ray spectra in large inorganic systems and metalloenzymes including those with multi-nuclear metal centers[118].
3) **Development of machine learning and other advanced algorithms to identify and correlate large data sets exhibiting small changes with subtle and/or complex time-**

dependent chemical and structural changes of the system under investigation. Advancements in machine learning algorithms have made a dramatic surge in recent years in online search engines and customer support, virtual personal assistants, live traffic predictions, video surveillance, social media services, email spam filtering, product recommendations and more. We need to learn how to develop similar approaches, to efficiently analyze and reduce our large and complex data sets that might contain 10^9 individual spectra from a single day of running an XFEL experiment. This is not simply doing the same analysis faster or on a larger scale, but requires spawning entirely new approaches that will extract the mechanistic understanding of catalytic reactions from the large XFEL data sets.

Understanding the function of metalloenzymes and molecular catalysts will greatly benefit from current and future XFELs and the X-ray methods described in this review. We hope that this work stimulates the readers to think about how these approaches can best benefit their research needs, and how we can further enhance them with the ultimate goal of bringing out the full potential of these powerful machines.

Sidebars:

Diffraction limit: The fundamental relationship between the size of a light source (D), the wavelength of the light (λ), and the divergence of the light beam (Δθ): $\Delta\theta \sim \lambda/\pi D$.

Emittance: Transverse emittance (ε) refers to the relationship between the angular spread (divergence) of an electron beam, and the transverse size of the beam, i.e. an area in phase space with dimensions of length x angle, $\varepsilon \sim \Delta\theta D$

Self-amplified spontaneous emission (SASE): The cooperative emission of X-rays from relativistic electrons propagating through a periodic array of magnets (undulator). The transverse undulating motion of the electrons in the magnetic field gives rise to spontaneous X-ray emission. Over a long propagation distance (~100 m) the X-ray field causes longitudinal microbunching of

the electrons at the X-ray wavelength, which in turn leads to stronger coherent emission, further microbunching, and exponential growth of the coherent X-ray emission.

Photon-in photon-out spectroscopy: X-ray spectroscopic methods, where photons incident on the sample ("photon-in") and photons leaving the sample are detected separately, to measure the X-ray spectroscopic observable ("photon-out"). The term applies to X-ray absorption spectroscopy (XAS) in transmission and fluorescence-yield mode, X-ray emission spectroscopy (XES), and resonant inelastic X-ray scattering (RIXS). The term is often used to distinguish from other modes of detection such as (Auger) electrons or ions. Due to the large penetration depth of X-rays compared to electrons or ions, photon-out detection is used for studying the bulk of condensed matter.

Fluorescence and Auger electron decay/yield: The decay of core-excited states by emission of an X-ray fluorescence photon or an Auger electron. X-ray fluorescence and Auger decays are competitive processes and their relative yield depends on the atomic number of the core-excited atom. In 3*d* transition metals, Auger decay dominates for L-edge excitation with a minor fluorescence decay channel (0.5% for Mn, e.g.[66]) whereas fluorescence decay dominates for K-edge excitation (31% for Mn, e.g.[66]).

Core-hole lifetime broadening: The (homogeneous) energy broadening of a core transition due to the finite lifetime of the core hole. For a Lorentzian line shape, this can be expressed as: $\Delta E_{FWHM} \Delta T_{1/e} = 0.6589$ eV fs, where ΔE_{FWHM} is the FWHM of the line width, and $\Delta T_{1/e}$ is the exponential lifetime (also referred to as dephasing time) of the corresponding core-excited state. Note that for an ensemble of emitters, the dephasing time represents the time within which the emission is in-phase.

Seeding: In laser physics, seeding is defined as process, where a signal (typically from a weak laser) is injected into a gain medium (typically from a strong laser) to improve the output signal by stabilizing the wavelength and reducing variations in the output pulse energy and timing (jitter) (Section 2.1). In the context of Section 5.1, a weak X-ray laser pulse *seeds* the stimulated X-ray

emission from a fluorescence line after a strong pump X-ray laser pulse created excited states in the sample.

Oxidation state: The oxidation state of an atom in a compound describes the degree to which the electron number of that atom has changed compared to the uncharged neutral form of the same atom. In case of redox reactions of first row transition metals these changes happen in the 3*d* shell and hence the oxidation state is directly related to the number of 3*d* electrons present.

Spin state: In transition metal complexes the spin state refers to the distribution of electrons in the valence shell. Often there are two distributions possible for the same number of electrons that can be described as low spin (LS) or high spin (HS) configuration having either a low or high number of unpaired electrons. The energy of the LS vs. HS configuration depends on the symmetry and nature of the ligands around the metal center as described by crystal field or ligand field theory.

Metal to Ligand Charge Transfer (MLCT) and Ligand to Metal Charge Transfer (LMCT): MLCT and LMCT excitations are special cases of CT excitations in metal complexes. MLCT excited states result from one-electron transitions where an electron is promoted from a metal- to a ligand-centered orbital (e.g. $t_{2g} \rightarrow \pi^*$). LMCT excited states result from one-electron transitions where an electron is promoted from a ligand- to a metal-centered orbital (e.g. $\pi^* \rightarrow t_{2g}$).

HOMO, LUMO: In molecular-orbital (MO) theory, the highest occupied molecular orbital (HOMO) and the lowest unoccupied molecular orbital (LUMO) denote the frontier orbitals of molecules.

Partial-fluorescence yield XAS: Measuring fluorescence as a function of incident photon energy is often denoted partial-fluorescence yield X-ray absorption spectroscopy (XAS) and it usually applies to soft X-rays. The most intense fluorescence decay following 2*p* core-excitation corresponds to $3d \rightarrow 2p$ transitions and it is usually this partial fluorescence yield that is measured at transition-metal L-edges.

Charge and spin densities: Each electron as a particle carries one unit of charge and one unit of spin (alpha/spin up or beta/spin down). In the ensemble averages as described by quantum-chemical calculations, however, charge and spin density distributions in a metal complex or in the active center of a metalloenzyme can differ in that alpha (spin up) and beta (spin down) electrons are differently distributed in space. In this context, oxidation or reduction of a metal center entail complex and independent redistributions of charge and spin to accommodate the missing or extra electron.

Ligand-field (LF) and charge-transfer (CT) excitations/transitions: The valence orbitals in metal complexes can often be classified as either being metal-centered (large amplitude on the metal, e.g. e_g and t_{2g} orbitals) or ligand centered (large amplitude on one or several ligands, σ/σ^* or π/π^* orbitals, where the asterisk * denotes anti-bonding/unoccupied orbitals). Ligand-field (LF) and charge transfer (CT) excitations are electronic excitations in metal complexes. LF excitations, often also denoted d-d excitations, refer to one-electron transitions between metal-centered orbitals (e.g. $t_{2g} \rightarrow e_g$). Charge-transfer (CT) excitations correspond to one-electron transitions between metal- and ligand-centered orbitals, evoking the notion that electron charge is transferred between the metal and the ligands (e.g. $t_{2g} \rightarrow \pi^*$, where π^* is an unoccupied ligand orbital).

Spontaneous emission: The process in which an atom or molecule in an electronic excited state relaxes to a lower-energy electronic state through the emission of a photon.

Stimulated emission: The process by which an incident photon of a given energy (or wavelength) triggers an electronic transition in an excited atom or molecule to a lower electronic state, resulting in an emitted photon with the same wavevector, energy, and phase as the incident photon.

Amplified spontaneous emission: The spontaneous emission in an ensemble of atoms or molecules, the majority of which are in an electronic excited state. In this scenario, initial spontaneous emission events trigger subsequent stimulated emission events along the propagation path, and the resulting amplified spontaneous emission signal grows exponentially.

Seeded stimulated emission: A variation of the stimulated emission process (see above), in which the incident photon is provided in the form of a coherent pulse. Photons with a specific wavelength stimulate the emission of photons with that same wavelength.

Quantum coupling: The coupling of electronic wavefunctions. As used here, this refers to the mixing of molecular orbitals.

Four-wave-mixing: A nonlinear optical (X-ray) process involving four electromagnetic fields (e.g. three input fields $\boldsymbol{E}_1$, $\boldsymbol{E}_2$, $\boldsymbol{E}_3$, contribution to the creation of a new polarization $\boldsymbol{P}$). In a formulation that describes the susceptibility $\chi_{nonlinear}$ in terms of a perturbation expansion, four-wave mixing is a third-order process: $\boldsymbol{P}^{(3)}=\chi^{(3)}\boldsymbol{E}_1\boldsymbol{E}_2\,\boldsymbol{E}_3$.

Box: X-ray Spectroscopy

X-ray spectroscopy is used to characterize electronic and geometric structures of elements in their chemical environment[166], and here we will focus on 3*d* TMs. It is element-selective because the binding energies of core-electrons are specific to each element[167]. It is sensitive to the chemical environment, which imposes small shifts on these binding energies[168,169]. By tuning the incident energy to a resonance, X-ray spectroscopy exhibits orbital specificity[87,119,170,171]. X-ray absorption spectroscopy (XAS) probes the electronic transitions from ground to core-excited states, while X-ray emission spectroscopy (XES) probes the fluorescence decay of core-excited states. The figure in this box shows a generalized energy level diagram for 3*d* TM systems for hard and soft X-ray spectroscopy. XAS and XES are complementary techniques providing information about local metal oxidation states, valence orbital populations and interactions, local metal spin states, ligand coordination, bond lengths and symmetry changes, and metal-ligand covalency.

XAS probes the transitions of a core electron to empty or partially unoccupied molecular orbitals with symmetries given by the dipole selection rule[170-174]. K-edge XAS (hard X-rays) probes predominantly unoccupied molecular orbitals with *p* symmetry via 1*s*→4*p* transitions. In the K pre-edge region, weak quadrupolar 1*s*→3*d* transitions can be observed, which gain intensity

through mixing with orbitals with *p* symmetry. L-edge XAS (soft X-rays) predominantly probes the orbitals with *d* symmetry via $2p \rightarrow 3d$ transitions. These transitions relate to the low-energy region of an XAS spectrum (first few eV in the soft X-ray range, and first few tens of an eV in the hard X-ray range) also called the X-ray absorption near edge structure (XANES) region. At higher energies (tens to hundreds of eV) is the extended X-ray absorption fine structure (EXAFS) region, which is dominated by scattering processes. Here the energy of the X-ray photons liberate photoelectrons that propagate from the absorber atom and are backscattered by neighboring atoms producing interferences and the characteristic EXAFS oscillations[175]. This signal provides information about the atomic number, distance, and coordination number of the atoms surrounding the metal absorber atom.

XES probes the transitions of an electron from an occupied orbital to an unoccupied or partially occupied core-orbital[176]. These transitions result from spontaneous fluorescence decays of core-excited states reached by X-ray absorption of the system. Non-resonant K XES (Kα, K$\beta_{1,3}$, $K\beta'$, $K\beta_{2,5}$ and $K\beta''$, see Figure (a)), where the excitation energy is well above the core electron binding energy, provides information on the metal oxidation state, effective spin, metal bonding orbitals, and nature of the ligand. L XES of 3*d* TMs and K XES of ligand atoms such as N or O provide sensitivity to oxidation states, symmetry, energies and interactions of occupied orbitals, and metal-ligand covalency.

Resonant inelastic X-ray scattering (RIXS) is a multidimensional X-ray spectroscopy offering enhanced electronic structural information[79,121,177,178]. In RIXS, the energy of photons scattered/emitted by the sample is measured with high spectral resolution, while the incident photon energy is scanned across the absorption edge. The corresponding 2D spectrum shows the incident photon energy versus that transferred to the sample, defined as the difference of incident and emitted/scattered photon energies. This energy transfer is in the range of meV-eV for soft X-ray RIXS corresponding to vibrational and valence-electronic *d-d* transitions, and up to several 100 eV for hard X-ray RIXS corresponding to resonant core-electron transitions. RIXS is the X-ray analog of resonance Raman scattering and provides the ability to probe the occupancy and interactions of both occupied and unoccupied orbitals in valence- and core-excited states.

In 1*s* RIXS, the incident hard X-ray energy is scanned across the K-pre-edge exciting 1*s* electrons to unoccupied 3*d*-derived valence orbitals, where $1s \rightarrow 3d$ transitions lead to $1s^1\ 3d^{n+1}$ intermediate states, and $2p^5 3d^{n+1}$, $3p^5 3d^{n+1}$ or $3d^{n*}$ final states, respectively (Figure (b))[121]. Therefore, 1*s* RIXS probes $2p \rightarrow 3d$ (similar to L-edge absorption), $3p \rightarrow 3d$ (similar to M-edge absorption), or valence-electron transitions with the advantages of hard X-rays.

In 2*p*3*d* RIXS, the incident soft X-ray energy is scanned across the L-edge exciting 2*p* electrons to unoccupied 3*d*-derived valence orbitals, where $2p \rightarrow 3d$ transitions lead to $2p^5 3d^{n+1}$ intermediate states, and $3d^{n*}$ final states (Figure (b))[121,179]. The energy transfer corresponds to valence-electron transitions of UV/Vis absorption, with the advantages of using an element-, chemical-site- and orbital-specific X-ray probe. 2*p*3*d* RIXS offers several additional advantages over UV/Vis absorption spectroscopy: It reveals *d-d* or ligand-field (LF) excitations over much wider energy ranges often hard to access with UV/Vis spectroscopy (down to below 1 eV and up to several 10 eV). LF or charge-transfer (CT) excitations can be selectively enhanced by resonant excitation, allowing to probe LF excitations unmasked from potentially overlapping CT transitions and solvent absorption that often dominate UV/Vis spectroscopy. Finally, due to spin-orbit interaction in the 2*p*-excited intermediate states, 2*p*3*d* RIXS allows probing transitions that are formally spin-forbidden in UV/Vis spectroscopy[121,179,180].

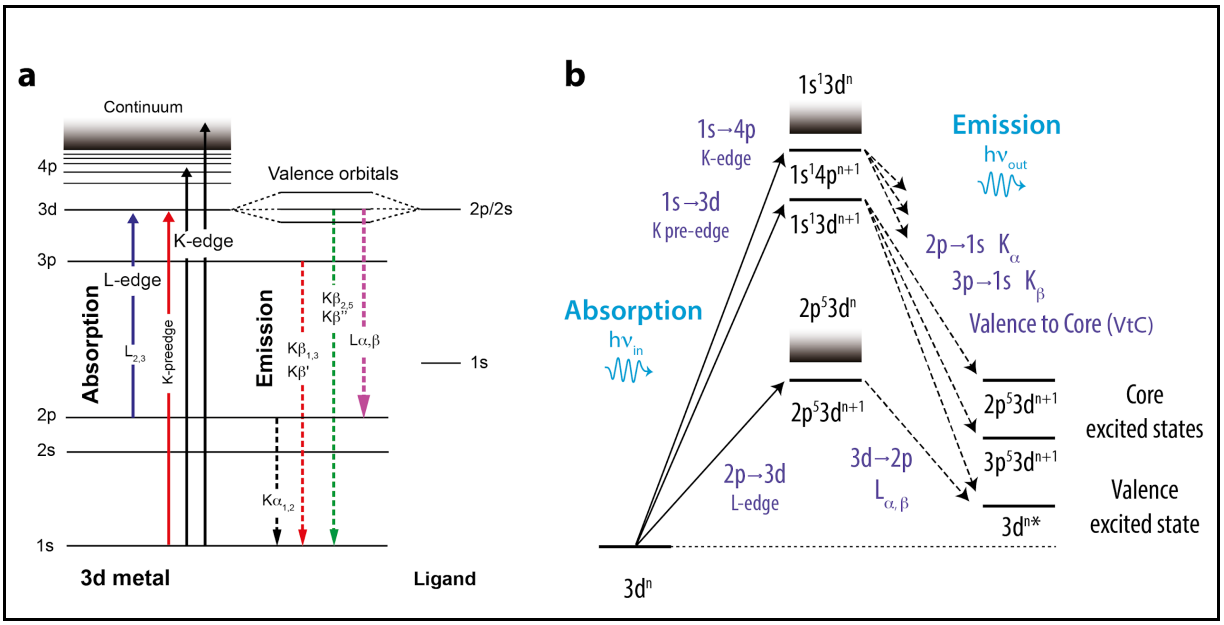

Figures

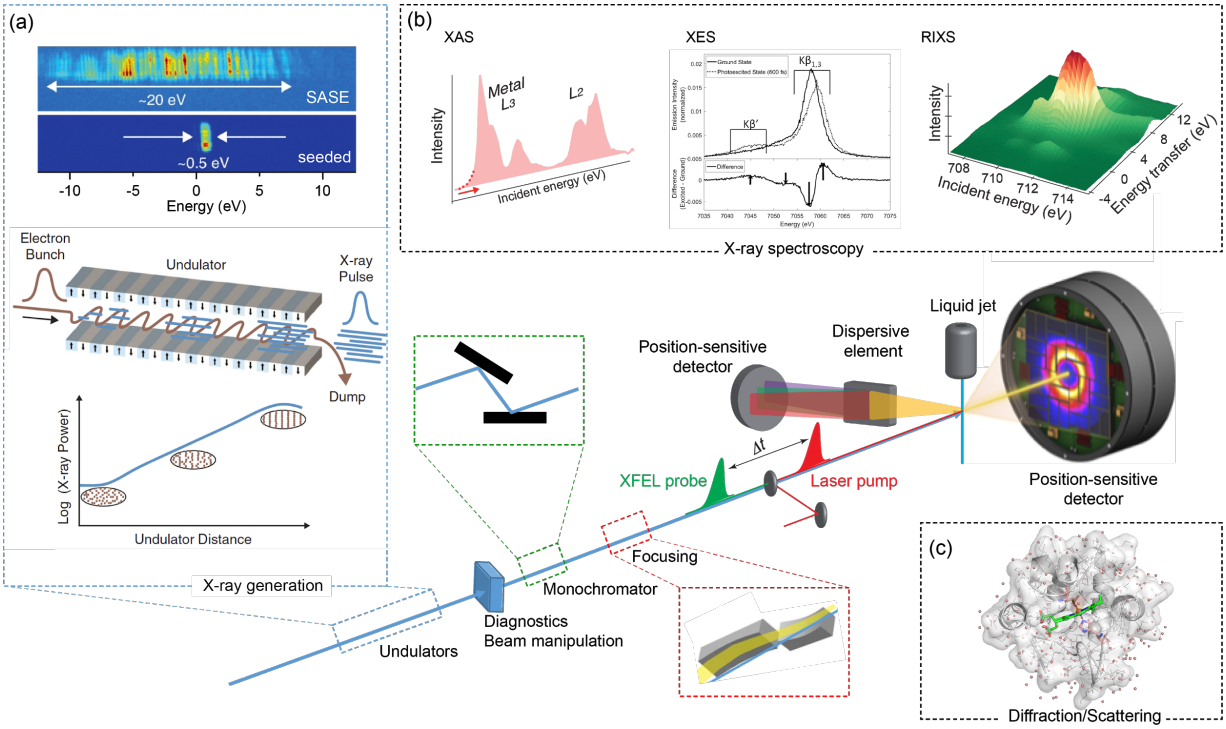

Figure 1: XFEL scheme and general experimental design for spectroscopy and diffraction/scattering experiments of metalloenzymes and molecular catalysts. Coherent X-rays are generated using relativistic electrons from a linear accelerator propagating through a periodic array of magnets (undulator). The transverse undulating motion of the electrons in the magnetic field gives rise to (spontaneous) X-ray emission. Over a long propagation distance (~100 m) the X-ray field causes microbunching of the electrons at the X-ray wavelength, which in turn leads to stronger coherent emission, further microbunching, and exponential growth of the coherent X-ray emission (**a,** bottom). At saturation, the X-ray pulses emitted from this self-amplified spontaneous emission (SASE) process have a relative bandwidth ($\Delta E/E_0$) of ~0.2% (a, top), with a pulse duration of a few to several tens of femtoseconds (**a**, top)(see Table 1). Diagnostics and beam manipulation provide ways to characterize and change properties of the XFEL beam, such as intensity or photon flux, beam position or pointing, X-ray spectrum, polarization, repetition rate,

pulse duration, and arrival time (note that not all these properties can be easily changed at every beamline at all XFELs). X-rays from the undulator are conditioned by beamline optics which typically include a monochromator (based on ruled gratings or Bragg crystals) and focusing mirrors. Narrower bandwidth (and higher spectral brightness) are achievable using self-seeding (**a**, top), whereby monochromatization is done upstream (between undulator segments), with further amplification in subsequent undulator segments. Samples are introduced at the focus of the X-ray beam, e.g. using a liquid injector or other methods to replace the sample volume at the repetition rate of the X-ray pulses. **b)** Numerous spectroscopy techniques are based on the detection of fluorescent X-rays (e.g. fluorescence detected XAS, XES, and RIXS), which are collected (in the direction orthogonal to the X-ray beam propagation) and analyzed by a spectrometer consisting of imaging optics and energy-selective elements (Bragg crystals for hard X-rays or dispersive ruled gratings for soft X-rays). **c)** X-rays scattered from molecular samples (or Bragg diffracted from crystalline samples) also contain important atomic structural information, and these are detected downstream with a position sensitive detector. As an example, the figure shows the cytochrome c structure (PDB: 6K9J). A part of the figure is adapted from refs. [19,58,181].

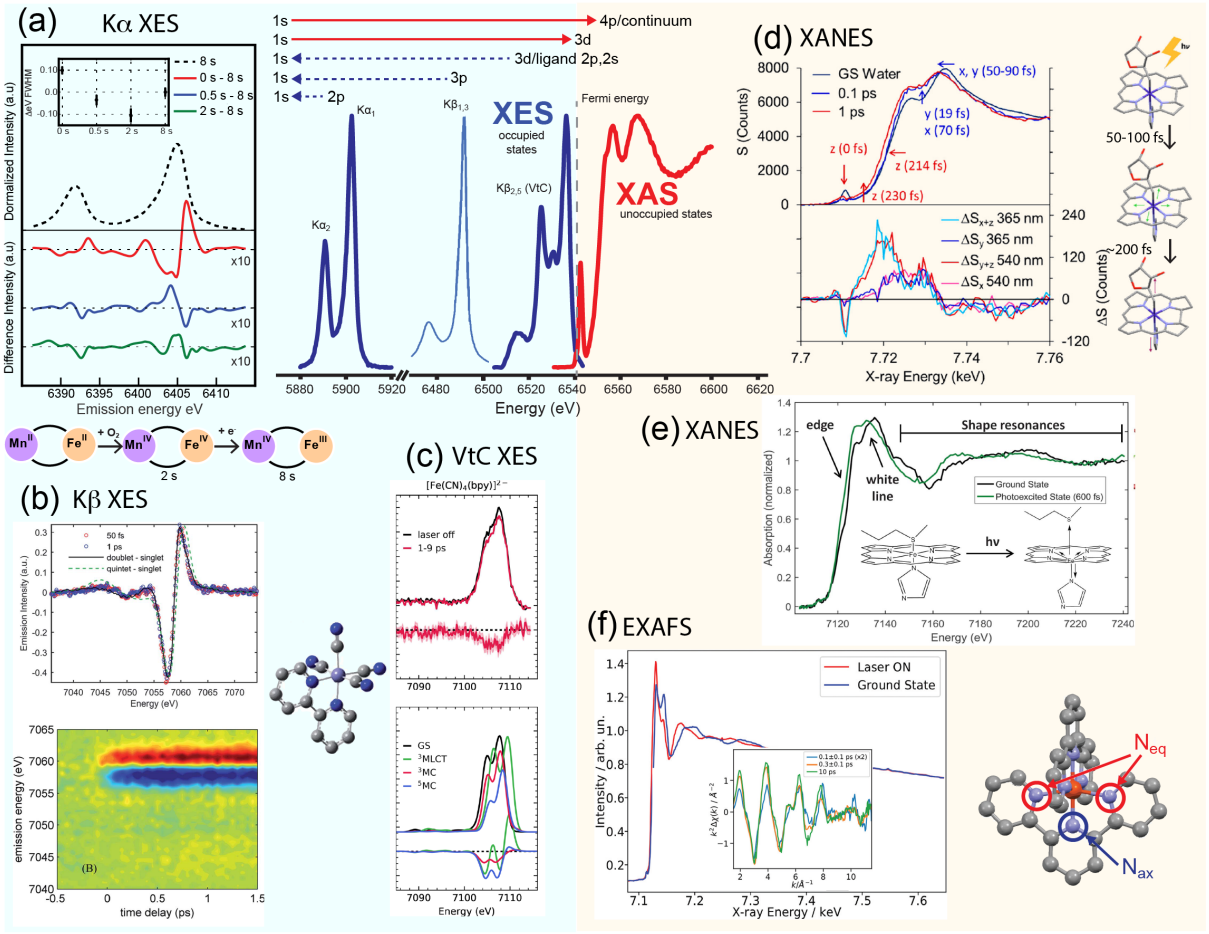

Figure 2: Hard X-ray spectroscopy at XFELs with a schematic view of the XES and XAS spectral region (for a Mn compound[182]) showing the complementarity of both methods in the center. **a)** Fe Kα XES of solutions of Fe/Mn containing ribonucleotide reductase R2c measured at LCLS at room temperature prior to O_2 incubation and changes observed after 0.5, 2 and 8 s *in-situ* O_2 incubation. A clear change in spectral shape and FWHM was found, indicating first formation of a Fe^{IV} intermediate (within ~2s) followed by the catalytically active Fe^{III} state[17]. **b)** Transient Fe Kb XES difference spectra of $Fe(bpy)(CN)_4$ (structure on the right) at 50 fs and 1ps after photoexcitation together with the calculated difference involving either a doublet MLCT or a quintet MC excited state (top) and contour plot (bottom) of light induced changes of the XES up to 1.5 ps after excitation[73]. The spectra indicate that likely only one excited state is present and the MLCT state is best fitting the data. **c)** Transient Fe VtC XES of $Fe(bpy)(CN)_4$ (top) and calculated spectra (bottom) showing clear light induced changes in the ps time range due to photooxidation and ligand dissociation[82]. **d)** Co XANES spectra of adenosine-cobalamin (structure shown to the right)

measured 0.1 and 1 ps after photo excitation (top) with features assigned to changes in the equatorial (x,y) or axial (z) direction indicated. In the bottom the changes in XANES 12 ps after excitation using different excitation polarization and wavelength of the excitation laser pulse are shown[91]. **e)** Time resolved XANES spectra of cytochrome c before and 600 fs after light excitation[58]. The changes in the edge position and the shape resonances were interpreted as an out of plane motion of the heme Fe coupled with a loss of the Fe-S(Met) bond. **f)** EXAFS spectra of $Fe(terpy)_2$ (inset). The k-space (right top) indicates light induced changes in the Fe-ligand distances in the sub-ps time scale. The potential energy surfaces which are involved in the ultrafast spin transition and time constants derived from the EXAFS measurements are shown in the schematic in the bottom[93].

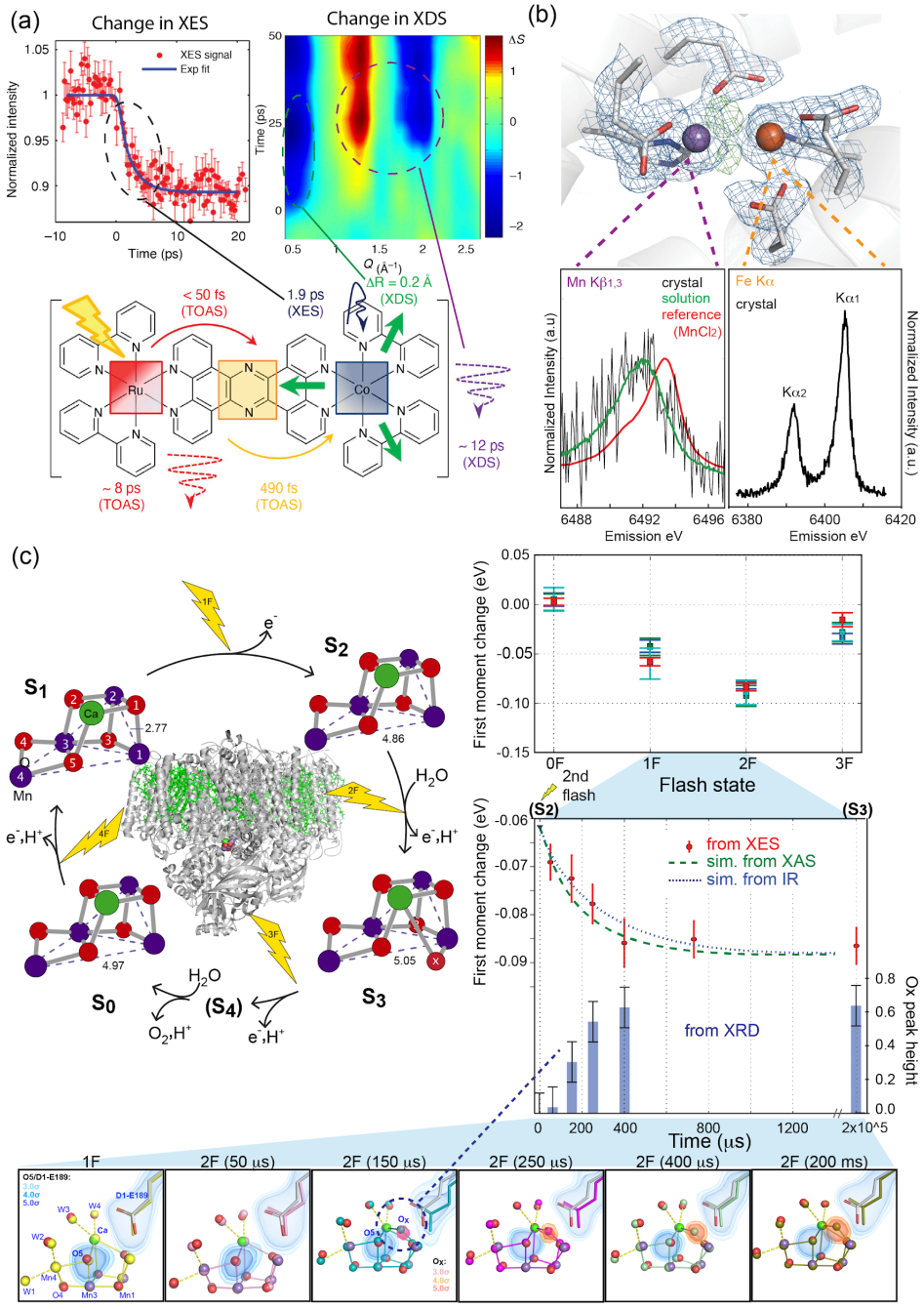

Figure 3: Multimodal detection methods applied for hard X-ray XFEL studies. **a)** Measurements of fs time resolved Kα XES (left) in parallel with XDS (right) on a Ru-Co dyad (bottom). The kinetics of the XES show the conversion of the LS to the HS form of Co within 2 ps while the XDS data exhibited a strong dip in intensity at 0.5 $Å^{-1}$ in the early time points, indicating an expansion by 0.2 Å in the 500 fs time scale and a 2nd feature indicating thermal equilibration at ~12 ps. In addition the scheme in the bottom contains information derived from transient optical

spectra, indicating ultrafast electron transfer from Ru to the bridge and transfer from the bridge to Co in <500 fs[97]. **b)** Combined XRD with Mn Kβ and Fe Kα XES of ribonucleotide reductase[17]. The structure of the dinuclear metal center as found in crystals of oxidized RNR is shown with Fe depicted as orange sphere and Mn as magenta sphere. Electron density is contoured at 1.2s in blue. Omit density (green) indicates the position of the bridging oxygen atoms. The Mn Kβ spectrum obtained from crystals (black) as well as from solutions (green) is shown together with a calibration spectrum of $Mn^{II}Cl_2$ (red) in the bottom left while the Fe Kα spectrum of the crystals is shown in the bottom right. **c)** Combined XRD and XES studies on PSII. The 5-step catalytic cycle (Kok cycle) together with the overall structure of the protein is shown on the left. For each stable state the XRD structure of the catalytic Mn_4Ca cluster obtained from XFEL measurements is shown as well[56]. Changes in the first moment of the Mn Kβ line measured in parallel are shown on the right top, indicating change in oxidation state of the Mn cluster by each illumination as expected. Results from time resolved XES and XRD measurements are shown in the bottom[57]. XRD and XES data show concomitant Mn oxidation and insertion of a new oxygen (Ox) in the Mn cluster (bottom) in the 250 μs time scale during the S_2 to S_3 state transition.

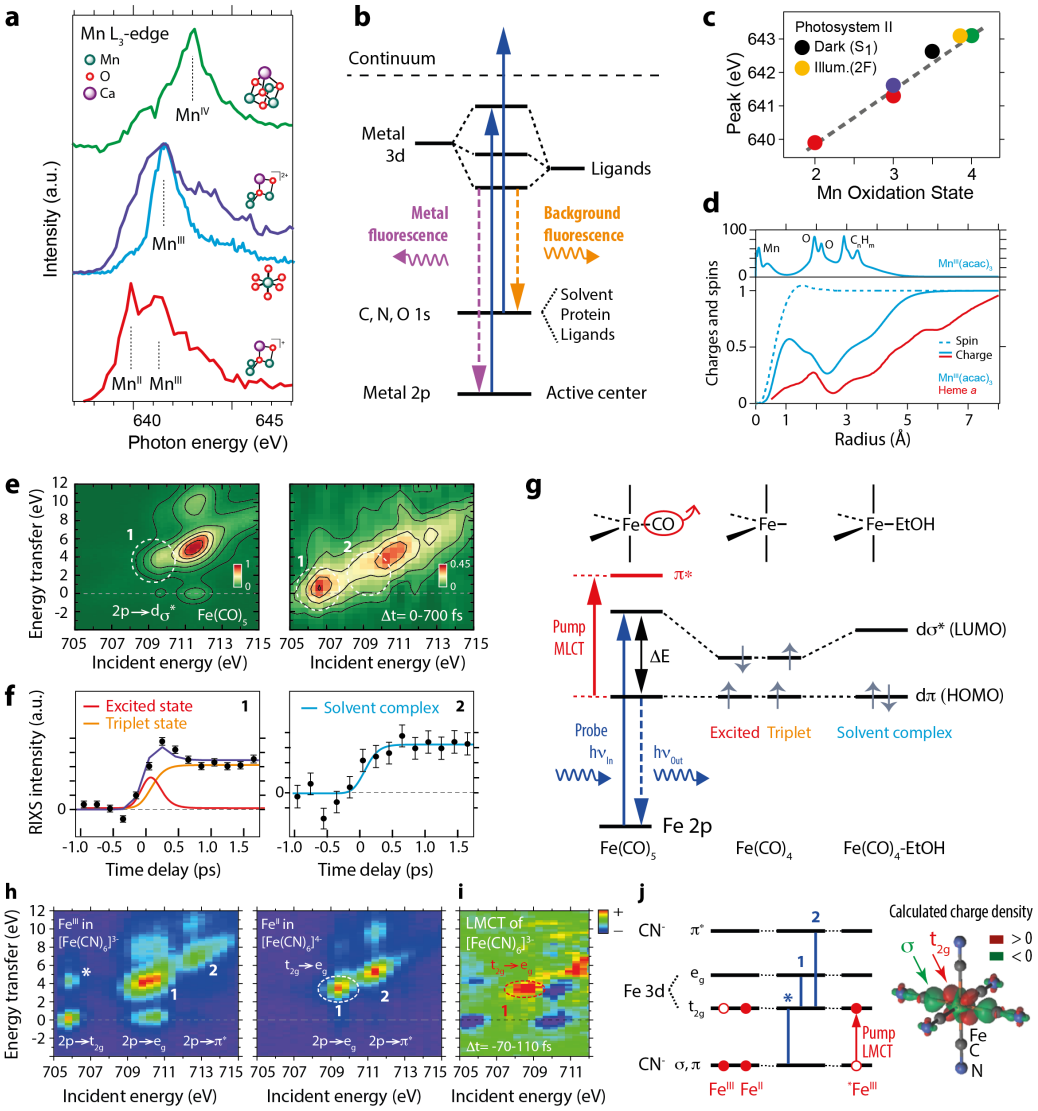

Figure 4. Soft X-ray spectroscopy at transition-metal L-edges with XFELs. **a)** Mn L-edge absorption spectra (L_3-edge partial fluorescence-yield spectra) and structures of non-cubane reduced $Mn^{II}Mn^{III}_2CaO(OH)$ (red), non-cubane oxidized $Mn^{III}_3CaO(OH)$ (dark blue), closed-cubane $Mn^{IV}_3CaO_4$ (all three measured in solution at the LCLS XFEL, Mn concentrations 6-15 mM, adapted from [13]), and of $Mn^{III}(acac)_3$ (light blue, measured in solution at the BESSY II synchrotron, Mn concentration 100 mM, adapted from [116]). **b)** Energy level diagram for metal-specific L-edge partial fluorescence-yield absorption spectroscopy. **c)** Mn L_3-edge peak maxima versus formal oxidation states for spectra of the inorganic compounds in **a** and for two states of the Mn_4CaO_5 cluster in photosystem II ($Mn^{III}_2Mn^{IV}_2CaO_5$ in the S_1 dark resting state and an S_3-enriched state with predominantly $Mn^{IV}_4CaO_5$ as obtained from illuminating photosystem II with two light flashes, spectra as measured at the LCLS XFEL at Mn concentrations of 0.8 mM not

shown, adapted from [13]). **d)** Calculated electron charge density in $Mn^{III}(acac)_3$ versus distance from the Mn center (top) and accumulated electron charge and spin densities upon reduction of $Mn^{III}(acac)_3$ and heme a versus distance from the Mn and Fe center, respectively (bottom, integrated radial charge and spin density differences for reduced minus oxidized forms reaching the value 1 when the equivalent of 1 charge/spin is reached in the integration, adapted from [116]). **e)** Measured resonant inelastic X-ray scattering (RIXS) intensities as a function of incident photon energy at the Fe L_3-edge and as a function of energy transfer (difference between incident and scattered photon energy) for $Fe(CO)_5$ (left) and averaged for pump-probe delay times of 0-700 fs after optical excitation of $Fe(CO)_5$ (right, measured in solution at the LCLS XFEL, Fe concentration 1 M, adapted from [119]). **f)** Integrated RIXS intensities as a function of pump-probe delay time for regions **1** and **2** as marked in **e** with a kinetic model (solid lines) relating measured RIXS intensities and populations of fitted species (adapted from [119]). **g)** Energy-level diagram for RIXS at the Fe L_3-edge of $Fe(CO)_5$ with optical excitation (metal to ligand charge transfer, MLCT, excitation initiating dissociation to $Fe(CO)_4$) and frontier-orbital energies and populations in excited- and triplet-state $Fe(CO)_4$ and $Fe(CO)_4$-ethanol (EtOH) solvent complexes (notations dπ and dσ are used to denominate Fe-centered 3*d*-derived orbitals of π and σ symmetry). **h)** Measured RIXS intensities at the Fe L_3-edge of ferric (Fe^{III}) and ferrous (Fe^{II}) iron hexacyanide $Fe(CN)_6$ (as measured in solution at the BESSY II synchrotron, Fe concentrations 0.5 and 0.33 M, respectively, adapted from [105]). **i**: Measured RIXS intensity differences averaged for pump-probe delay times of -70 to 110 fs after optical excitation of Fe^{III}-cyanide (right, pumped minus unpumped, representative of the ligand to metal charge transfer, LMCT, excited state of Fe^{III}-cyanide with respect to ground-state Fe^{III}-cyanide, measured in solution at the LCLS XFEL, integration was for -70 to 110 fs because temporal resolution in the experiment was 180 fs, Fe concentration 0.3 M, adapted from [123], saturated intensities are shown for better visualization in contrast to the raw intensities in [123]). **j)** Energy-level diagram in octahedral (O_h) symmetry for Fe^{III}- and Fe^{II}-cyanide and the LMCT state of ferric hexacyanide ($^*Fe^{III}$) with main RIXS transitions (*, 1, and 2 as indicated in **h** and **i**) and calculated electron charge density difference between LMCT $^*Fe^{III}$- and Fe^{III}-cyanide (LMCT minus ground state).

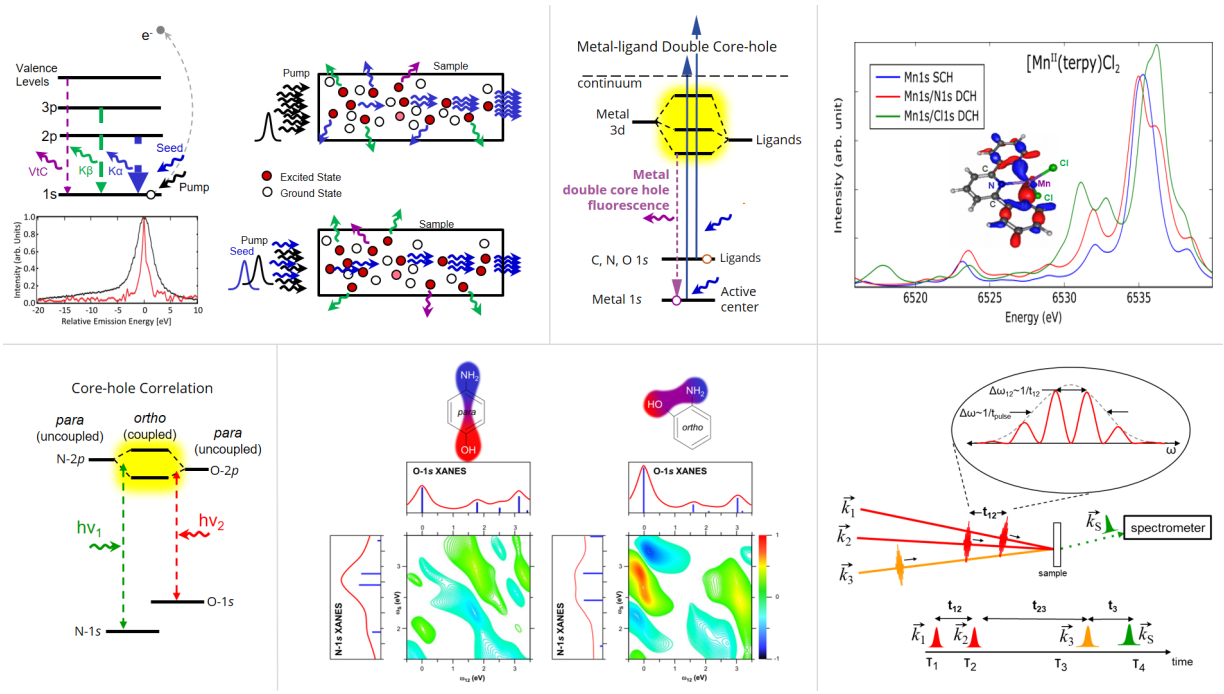

Figure 5.

Examples of future XFEL-based non-linear spectroscopy methods. **a)** Level diagram of various transition metal K emission lines and schematics of amplified spontaneous emission (top right) and seeded stimulated emission (bottom right). The pump pulse is tuned above the K edge to create 1s core hole excited states in the sample (red dots). In amplified spontaneous emission, a randomly forward emitted photon stimulates emission when encountering an excited atom leading to an amplification along the direction of the atoms in the excited states. In seeded stimulated emission, the seed pulse energy is tuned to that of the emission line that one wants to enhance along the pump/seed pulse direction. Bottom left: Single-shot seeded Kβ S-XES spectrum (red) of $NaMnO_4$ compared to conventional XES spectrum (black line), showing the potential for spectral narrowing in S-XES (Adapted from[138].) **b)** Level diagram and calculated VtC spectra in metal-ligand double core-hole XES. Two photons from the XFEL pulse simultaneously create a DCH state with one core hole in the metal and one in the ligand (left). The VtC XES spectrum in the presence of the ligand hole is modified, providing additional bonding information. Calculated DCH spectra with N (red) and Cl (green) are compared to the conventional SCH VtC spectrum of $Mn^{II}(terpy)Cl_2$ (right). **c)** Level diagram and representative calculated 2D XCCS maps for the *para* and *ortho* isomers of aminophenol. The degree of orbital mixing of the N-2*p* and O-2*p* valence states gives rise to a nonlinear mixing of the polarizations associated with resonant excitation from O-1*s* and N-1*s* core-levels. The off-diagonal cross-peaks (right map) indicates the enhanced mixing in the

ortho conformation (effectively mixing of the N-1*s* and O-1*s* XANES spectra). Such quantum effects are absent in the *para* isomer due to the separation of the O and N atoms (adapted from ref.[160]). **d)** Generalized schematic of XCCS using a four-wave mixing geometry with a three-pulse sequence (k_1, k_2, k_3). The signal of interest is the nonlinear polarization, k_S, shown here resolved in frequency (energy) using a spectrometer. The other energy axis (ω_{12}) is determined by the Fourier transform of the signal with respect to the time delays of the first two phase-locked pulses.

Table 1. Characteristic parameter of the various XFEL facilities worldwide (adapted from ref [183])**:**

Country	Facility Name	Photon energy (keV)	Pulse length[a] (fs)	Pulse energy[b] (mJ)	Rep rate (Hz)	Flux (ph/s)[f]	Start of operation
Japan	SACLA BL2,3	4-20	2-10	0.1-1	60	2-9x10^{13}	2011
	SACLA BL1	0.04-0.15	60	0.1	60	3-9x10^{14}	2015
Italy	FERMI FEL-1	0.01-0.06	40-90	0.08-0.2	10 (50)	1-6x10^{15}	2010
	FERMI FEL-2	0.06-0.3	20-50	0.01-0.1	10 (50)	1-5x10^{14}	2012
Germany	FLASH1	0.02-0.3	50-200	0.03-0.5	(1-800)x10[c]	0.08-1x10^{18}	2005
	FLASH2	0.01-0.3	50-200	0.03-0.3	(1-800)x10	0.05-2x10^{18}	2015
Korea	PAL-XFEL	2.5-15	5-50	0.8-1.5	60	0.4-2x10^{14}	2016
		0.25-1.2	5-50	0.2	60	0.6-3x10^{14}	2016
Switzerland	SwissFEL	1.8-12.4	10-70	1	100	0.5-3x10^{14}	2017
		0.2-2	10-70	1	100	0.3-3x10^{15}	2021
Europe	XFEL-SASE1,2	3-25	10-100	2	2,700x10[d]	0.1-1x10^{17}	2017
	XFEL-SASE3	0.2-3	10-100	2	2,700x10	0.1-2x10^{18}	2017
USA	LCLS	0.3-12	2-500	2-4	120	0.03-1x10^{16}	2009
	LCLS-II	1-25	10-100	2-4	120	0.1-3x10^{15}	2022[e]
	LCLS-II	0.2-5	10-200	0.02-1	10^6	0.04-1x10^{19}	2022[e]
	LCLS-II-HE	0.2-13	10-200	0.02-1	10^6	0.01-1x10^{19}	2026[e]

[a] Estimated pulse length (FWHM) based on e-bunch length measurement or designed range.

[b] Rough estimates of pulse energy, particularly for projects that are currently under construction.

[c] Burst mode operation at 10 Hz, with each macropulse providing up to 800 bunches at 1 MHz.

[d] Pulsed mode operation at 10 Hz, with each macropulse providing up to 2700 bunches at 5 MHz.

[e] Projected project completion dates.

[f] Flux (ph/s) is based on the combination of maximum pulse energy and repetition rate, and the range reflects the range of photon energies available from that source. Note that for LCLS-II and LCLS-II-HE the pulse energy (as a function of repetition rate) is constant up to ~300 kHz, and scales inversely with repetition rate above ~300 kHz.

Acknowledgements

J.K., V.K.Y., and J.Y. thank the support from the Director, Office of Science, Office of Basic Energy Sciences (OBES), Division of Chemical Sciences, Geosciences, and Biosciences (CSGB) of the Department of Energy (DOE) under contract DE-AC02-05CH11231. The National Institutes of Health (NIH) provides funding through Grants GM126289 (J.K.), GM110501 (J.Y.) for instrumentation development for XFEL experiments and metalloenzyme studies, and GM055302 (V.K.Y.) for biochemical aspects of PS II research. This work was supported by the US Department of Energy, Office of Science, Basic Energy Sciences under Contract no. DEAC02-76SF00515 (U.B., R.S.). Ph.W. is grateful to Raphael Jay for providing access to some of the data in Figure 4 and for fruitful discussions.

Author contributions

The authors contributed equally to all aspects of the article.

Key References

13 Kubin 2017: This first Mn L-edge soft x-ray spectroscopic study of photosystem II at physiological (in operando) conditions based on measurements at the LCLS XFEL establishes protocols for “probe-before-destroy” spectroscopy of dilute high-valent metal complexes and proteins at XFELs.

57 Ibrahim 2020: The application of combined X-ray crystallography and X-ray emission spectroscopy at an XFEL to understand the sequence of events during the water oxidation reaction in photosystem II.

68 Zhang 2014: In this study it was demonstrated that fs time resolution Fe K-edge X-ray emission spectroscopy can be used to investigate ultrafast spin-crossover dynamics in transition metal systems resulting from photo-induced metal-to-ligand charge transfer excitation.

88 Katayama 2019: This study on the femtosecond excited-state dynamics of a Cu complex in solution based on time-resolved Cu K-edge hard x-ray absorption spectroscopy at the SACLA XFEL reports the observation of hitherto undetected nuclear wavepacket dynamics and a new mechanism for the ultrafast relaxation in the photochemical reaction of this complex.

119 Wernet 2015: This first femtosecond time-resolved resonant inelastic x-ray scattering (RIXS) study of a metal complex in solution based on Fe L-edge soft x-ray measurements at the LCLS XFEL establishes probing photo-activated metal complexes in solution with XFELs and motivates using XFEL pulses for probing ultrafast dynamics in photocatalysts.

122 Hocking 2006: This classical study is exemplary for the use of transition-metal L-edge soft X-ray spectroscopy for element- and chemical-site selective and orbital-specific probing of the electronic structure of metal complexes and it details how the covalence of metal-ligand bonds can be quantified.

134 Rohringer 2012: In this study the first observation of an atomic inner-shell X-ray laser, creating strong gain of x-ray emission in the forward direction is reported.

137 Kroll 2018: A study of using stimulated x-ray emission as a novel spectroscopy tool to study transition metal complexes.

159 Mukamel 2009: A review of multidimensional spectroscopy techniques with an outlook to future XFEL application.

References

1 Röntgen, W. C. On a new kind of rays. *Science* **3**, 227-231, doi:10.1126/science.3.59.227 (1896).

2 Watson, J. D. & Crick, F. H. C. Molecular Structure of Nucleic Acids - a Structure for Deoxyribose Nucleic Acid. *Nature* **171**, 737-738, doi:10.1038/171737a0 (1953).

3 Rossbach, J., Schneider, J. R. & Wurth, W. 10 years of pioneering X-ray science at the Free-Electron Laser FLASH at DESY. *Phys Rep* **808**, 1-74, doi:10.1016/j.physrep.2019.02.002 (2019).

4 Garman, E. F. Radiation damage in macromolecular crystallography: what is it and why should we care? *Acta Cryst D Biol Crystallogr* **66**, 339-351, doi:10.1107/S0907444910008656 (2010).

5 March, A. M. *et al.* Development of high-repetition-rate laser pump/x-ray probe methodologies for synchrotron facilities. *Rev Sci Instrum* **82**, 073110, doi:10.1063/1.3615245 (2011).

6 Borfecchia, E., Garino, C., Salassa, L. & Lamberti, C. Synchrotron ultrafast techniques for photoactive transition metal complexes. *Philos Trans A Math Phys Eng Sci* **371**, 20120132, doi:10.1098/rsta.2012.0132 (2013).

7 Smolentsev, G. *et al.* Pump-probe XAS investigation of the triplet state of an Ir photosensitizer with chromenopyridinone ligands. *Photochem Photobiol Sci* **17**, 896-902, doi:10.1039/c8pp00065d (2018).

8 Chaussavoine, I. *et al.* The microfluidic laboratory at Synchrotron SOLEIL. *J Synchrotron Radiat* **27**, 230-237, doi:10.1107/S1600577519015042 (2020).

9 Monteiro, D. C. F. *et al.* 3D-MiXD: 3D-printed X-ray-compatible microfluidic devices for rapid, low-consumption serial synchrotron crystallography data collection in flow. *IUCrJ* **7**, 207-219, doi:10.1107/S2052252519016865 (2020).

10 Neutze, R., Wouts, R., van der Spoel, D., Weckert, E. & Hajdu, J. Potential for biomolecular imaging with femtosecond X-ray pulses. *Nature* **406**, 752-757, doi:10.1038/35021099 (2000).

11 Chapman, H. N. *et al.* Femtosecond X-ray protein nanocrystallography. *Nature* **470**, 73-77, doi:Doi 10.1038/Nature09750 (2011).

12 Alonso-Mori, R. *et al.* Energy-dispersive X-ray emission spectroscopy using an X-ray free-electron laser in a shot-by-shot mode. *Proc. Natl. Acad. Sci. U. S. A.* **109**, 19103-19107, doi:10.1073/pnas.1211384109 (2012).

13 Kubin, M. *et al.* Soft x-ray absorption spectroscopy of metalloproteins and high-valent metal-complexes at room temperature using free-electron lasers. *Struct Dynam* **4**, 054307, doi:10.1063/1.4986627 (2017).

14 Weierstall, U. Liquid sample delivery techniques for serial femtosecond crystallography. *Philos Trans R Soc Lond B Biol Sci* **369**, 20130337, doi:10.1098/rstb.2013.0337 (2014).

15 Sierra, R. G. *et al.* Concentric-flow electrokinetic injector enables serial crystallography of ribosome and photosystem II. *Nat Methods* **13**, 59-62, doi:10.1038/nmeth.3667 (2016).

16 Deponte, D. in *X-Ray Free Electron Lasers: Applications in Materials, Chemistry and Biology Energ y and Environment Series* (eds U. Bergmann, V. K. Yachandra, & J. Yano) Ch. 16, 325-336 (Royal Society of Chemistry, 2017).

17 Fuller, F. D. *et al.* Drop-on-demand sample delivery for studying biocatalysts in action at X-ray free-electron lasers. *Nat Methods* **14**, 443-449, doi:10.1038/nmeth.4195 (2017).

18 Martiel, I., Müller-Werkmeister, H. M. & Cohen, A. E. Strategies for sample delivery for femtosecond crystallography. *Acta Cryst D Struct Biol* **75**, 160-177, doi:10.1107/s2059798318017953 (2019).

19 Bostedt, C. *et al.* Linac Coherent Light Source: The first five years. *Rev Mod Phys* **88**, doi:10.1103/RevModPhys.88.015007 (2016).

20 Zhu, D. *et al.* A single-shot transmissive spectrometer for hard x-ray free electron lasers. *Applied Phys Lett* **101**, doi:10.1063/1.4736725 (2012).

21 Harmand, M. *et al.* Achieving few-femtosecond time-sorting at hard X-ray free-electron lasers. *Nat Photonics* **7**, 215-218, doi:10.1038/nphoton.2013.11 (2013).

22 Tono, K. *et al.* Beamline, experimental stations and photon beam diagnostics for the hard x-ray free electron laser of SACLA. *New J Phys* **15**, 083025, doi:10.1088/1367-2630/15/8/083035 (2013).

23 Elsaesser, T. Introduction: Ultrafast Processes in Chemistry. *Chem Rev* **117**, 10621-10622, doi:10.1021/acs.chemrev.7b00226 (2017).

24 Marangos, J. P. The measurement of ultrafast electronic and structural dynamics with X-rays. *Philos Trans A Math Phys Eng Sci* **377**, 20170481, doi:10.1098/rsta.2017.0481 (2019).

25 Asakura, K., Gaffney, K. J., Milne, C. & Yabashi, M. XFELs: cutting edge X-ray light for chemical and material sciences. *Phys Chem Chem Phys* **22**, 2612-2614, doi:10.1039/c9cp90304f (2020).

26 Milne, C. J., Penfold, T. J. & Chergui, M. Recent experimental and theoretical developments in time-resolved X-ray spectroscopies. *Coord Chem Rev* **277-278**, 44-68, doi:10.1016/j.ccr.2014.02.013 (2014).

27 Kondratenko, A. M. & Saldin, E. L. Generation of Coherent Radiation by a Relativistic Electron Beam in an Undulator. *Part. Accel.* **10**, 207-216 (1980).

28 Bonifacio, R., Pellegrini, C. & Narducci, L. M. Collective Instabilities and High-Gain Regime in a Free-Electron Laser. *Opt Commun* **50**, 373-378, doi:Doi 10.1016/0030-4018(84)90105-6 (1984).

29 Allaria, E. *et al.* The FERMI free-electron lasers. *J Synchrotron Radiat* **22**, 485-491, doi:doi:10.1107/S1600577515005366 (2015).

30 Ishikawa, T. *et al.* A compact X-ray free-electron laser emitting in the sub-angstrom region. *Nat Photon* **6**, 540-544 (2012).

31 Ko, I. S. *et al.* Construction and Commissioning of PAL-XFEL Facility. *Applied Sciences* **7**, 479 (2017).

32 Milne, C. *et al.* SwissFEL: The Swiss X-ray Free Electron Laser. *Applied Sciences* **7**, 720 (2017).

33 Ayvazyan, V. *et al.* First operation of a free-electron laser generating GW power radiation at 32 nm wavelength. *Eur. Phys. J. D* **37**, 297-303 (2006).

34 Tschentscher, T. *et al.* Photon Beam Transport and Scientific Instruments at the European XFEL. *Applied Sciences* **7**, 592, doi:10.3390/app7060592 (2017).

35 LCLS-II Conceptual Design Report. 519 (2014).

36 Linac Coherent Light Source II High Energy Upgrade (LCLS-II-HE) Conceptual Design Report - SLAC-R-1098. (SLAC National Accelerator Laboratory, https://slacspace.slac.stanford.edu/sites/lcls/lcls-2-he/cdr/LCLS-II-HE%20CDR%20March%2023%202018.pdf, 2017).

37 Huang, S. *et al.* Generating Single-Spike Hard X-Ray Pulses with Nonlinear Bunch Compression in Free-Electron Lasers. *Phys Rev Lett* **119**, 154801, doi:10.1103/PhysRevLett.119.154801 (2017).

38 Duris, J. *et al.* Tunable isolated attosecond X-ray pulses with gigawatt peak power from a free-electron laser. *Nat Photonics* **14**, 30-36, doi:10.1038/s41566-019-0549-5 (2019).

39 Amann, J. *et al.* Demonstration of self-seeding in a hard-X-ray free-electron laser. *Nat Photonics* **6**, 693-698, doi:10.1038/nphoton.2012.180 (2012).

40 Allaria, E. *et al.* Highly coherent and stable pulses from the FERMI seeded free-electron laser in the extreme ultraviolet. *Nat Photonics* **6**, 699-704, doi:10.1038/nphoton.2012.233 (2012).

41 Allaria, E. *et al.* Two-colour pump-probe experiments with a twin-pulse-seed extreme ultraviolet free-electron laser. *Nat Comm* **4**, 2476, doi:10.1038/ncomms3476 (2013).

42 Ackermann, S. *et al.* Generation of coherent 19- and 38-nm radiation at a free-electron laser directly seeded at 38 nm. *Phys Rev Lett* **111**, 114801, doi:10.1103/PhysRevLett.111.114801 (2013).

43 Ratner, D. *et al.* Experimental demonstration of a soft x-ray self-seeded free-electron laser. *Phys Rev Lett* **114**, 054801, doi:10.1103/PhysRevLett.114.054801 (2015).

44 Gauthier, D. *et al.* Generation of Phase-Locked Pulses from a Seeded Free-Electron Laser. *Phys Rev Lett* **116**, 024801, doi:10.1103/PhysRevLett.116.024801 (2016).

45 Finetti, P. *et al.* Pulse Duration of Seeded Free-Electron Lasers. *Phys Rev X* **7**, doi:10.1103/PhysRevX.7.021043 (2017).

46 Inoue, I. *et al.* Generation of narrow-band X-ray free-electron laser via reflection self-seeding. *Nat Photonics* **13**, 319-322, doi:10.1038/s41566-019-0365-y (2019).

47 Hara, T. *et al.* Two-colour hard X-ray free-electron laser with wide tunability. *Nat Commun* **4**, 2919, doi:10.1038/ncomms3919 (2013).

48 Lutman, A. A. *et al.* Experimental demonstration of femtosecond two-color x-ray free-electron lasers. *Phys Rev Lett* **110**, 134801, doi:10.1103/PhysRevLett.110.134801 (2013).

49 Marinelli, A. *et al.* Multicolor operation and spectral control in a gain-modulated x-ray free-electron laser. *Phys Rev Lett* **111**, 134801, doi:10.1103/PhysRevLett.111.134801 (2013).

50 Lutman, A. A. *et al.* Demonstration of single-crystal self-seeded two-color x-ray free-electron lasers. *Phys Rev Lett* **113**, 254801, doi:10.1103/PhysRevLett.113.254801 (2014).

51 Marinelli, A. *et al.* High-intensity double-pulse X-ray free-electron laser. *Nat Commun* **6**, 6369, doi:10.1038/ncomms7369 (2015).

52 Prince, K. C. *et al.* Coherent control with a short-wavelength free-electron laser. *Nat Photonics* **10**, 176-179, doi:10.1038/nphoton.2016.13 (2016).

53 Hartmann, N. *et al.* Attosecond time–energy structure of X-ray free-electron laser pulses. *Nat Photonics* **12**, 215-220, doi:10.1038/s41566-018-0107-6 (2018).

54 Kraus, P. M., Zürch, M., Cushing, S. K., Neumark, D. M. & Leone, S. R. The ultrafast X-ray spectroscopic revolution in chemical dynamics. *Nat Rev Chem* **2**, 82-94, doi:10.1038/s41570-018-0008-8 (2018).

55 Kern, J. *et al.* Simultaneous femtosecond X-ray spectroscopy and diffraction of photosystem II at room temperature. *Science* **340**, 491-495, doi:10.1126/science.1234273 (2013).

56 Kern, J. *et al.* Structures of the intermediates of Kok's photosynthetic water oxidation clock. *Nature* **563**, 421-425, doi:10.1038/s41586-018-0681-2 (2018).

57 Ibrahim, M. *et al.* Untangling the sequence of events during the S_2 --> S_3 transition in photosystem II and implications for the water oxidation mechanism. *Proc. Natl. Acad. Sci. U. S. A.* **117**, 12624-12635, doi:10.1073/pnas.2000529117 (2020).

58 Mara, M. W. *et al.* Metalloprotein entatic control of ligand-metal bonds quantified by ultrafast x-ray spectroscopy. *Science* **356**, 1276-1280, doi:10.1126/science.aam6203 (2017).

59 Bacellar, C. *et al.* Spin cascade and doming in ferric hemes: Femtosecond X-ray absorption and X-ray emission studies. *Proc. Natl. Acad. Sci. U. S. A.* **117**, 21914-21920, doi:10.1073/pnas.2009490117 (2020).

60 Kinschel, D. *et al.* Femtosecond X-ray emission study of the spin cross-over dynamics in haem proteins. *Nat Commun* **11**, 4145, doi:10.1038/s41467-020-17923-w (2020).

61 Schreck, S. *et al.* Reabsorption of soft x-ray emission at high x-ray free-electron laser fluences. *Phys Rev Lett* **113**, 153002, doi:10.1103/PhysRevLett.113.153002 (2014).

62 Szlachetko, J. *et al.* Establishing nonlinearity thresholds with ultraintense X-ray pulses. *Sci Rep* **6**, 33292, doi:10.1038/srep33292 (2016).

63 Tamasaku, K. *et al.* X-ray two-photon absorption competing against single and sequential multiphoton processes. *Nat Photonics* **8**, 313-316, doi:10.1038/nphoton.2014.10 (2014).

64 Spence, J. C. H. Outrunning damage: Electrons vs X-rays-timescales and mechanisms. *Struct Dyn* **4**, 044027, doi:10.1063/1.4984606 (2017).

65 Alonso-Mori, R. Femtosecond electronic structure response to high intensity XFEL pulses probed by iron X-ray emission spectroscopy. *Scientific Reports*, doi:10.1038/s41598-020-74003-1 (2020).

66 Krause, M. O. & Oliver, J. H. Natural widths of atomic K and L levels, Kα X-ray lines and several KLL Auger lines. *J Physi Chem Ref Data* **8**, 329-338, doi:10.1063/1.555595 (1979).

67 Neeb, M., Rubensson, J. E., Biermann, M. & Eberhardt, W. Coherent excitation of vibrational wave functions observed in core hole decay spectra of O_2, N_2 and CO. *J Elec Spect Rel Phen* **67**, 261-274, doi:10.1016/0368-2048(93)02050-v (1994).

68 Zhang, W. *et al.* Tracking excited-state charge and spin dynamics in iron coordination complexes. *Nature* **509**, 345-348, doi:10.1038/nature13252 (2014).

69 Haldrup, K. *et al.* Observing Solvation Dynamics with Simultaneous Femtosecond X-ray Emission Spectroscopy and X-ray Scattering. *J Phys Chem B* **120**, 1158-1168, doi:10.1021/acs.jpcb.5b12471 (2016).

70 Kubin, M. *et al.* Direct determination of absolute absorption cross sections at the L-edge of dilute Mn complexes in solution using a transmission flatjet. *Inorg. Chem.* **57**, 5449-5462, doi:10.1021/acs.inorgchem.8b00419 (2018).

71 Fransson, T. *et al.* X-ray emission spectroscopy as an in situ diagnostic tool for X-ray crystallography of metalloproteins using an X-ray free-electron laser. *Biochemistry* **57**, 4629-4637 (2018).

72 Srinivas, V. *et al.* High Resolution XFEL Structure of the Soluble Methane Monooxygenase Hydroxylase Complex with its Regulatory Component at Ambient Temperature in Two Oxidation States. *J Am Chem Soc*, doi:10.1021/jacs.0c05613 (2020).

73 Zhang, W. *et al.* Manipulating charge transfer excited state relaxation and spin crossover in iron coordination complexes with ligand substitution. *Chem Sci* **8**, 515-523, doi:10.1039/c6sc03070j (2017).

74 Kjaer, K. S. *et al.* Ligand manipulation of charge transfer excited state relaxation and spin crossover in [Fe(2,2'-bipyridine)$_2$(CN)$_2$]. *Struct Dyn* **4**, 044030, doi:10.1063/1.4985017 (2017).

75 Kjaer, K. S. *et al.* Finding intersections between electronic excited state potential energy surfaces with simultaneous ultrafast X-ray scattering and spectroscopy. *Chem Sci* **10**, 5749-5760, doi:10.1039/c8sc04023k (2019).

76 Tatsuno, H. *et al.* Hot Branching Dynamics in a Light-Harvesting Iron Carbene Complex Revealed by Ultrafast X-ray Emission Spectroscopy. *Angew Chem Int Ed Engl* **59**, 364-372, doi:10.1002/anie.201908065 (2020).

77 Kunnus, K. *et al.* Vibrational wavepacket dynamics in Fe carbene photosensitizer determined with femtosecond X-ray emission and scattering. *Nat Commun* **11**, 634, doi:10.1038/s41467-020-14468-w (2020).

78 Vacher, M., Kunnus, K., Delcey, M. G., Gaffney, K. J. & Lundberg, M. Origin of core-to-core x-ray emission spectroscopy sensitivity to structural dynamics. *Struct Dyn* **7**, 044102, doi:10.1063/4.0000022 (2020).

79 Glatzel, P. & Bergmann, U. High resolution 1s core hole X-ray spectroscopy in 3d transition metal complexes—electronic and structural information. *Coord Chem Rev* **249**, 65-95, doi:10.1016/j.ccr.2004.04.011 (2005).

80 Pollock, C. J. & DeBeer, S. Insights into the geometric and electronic structure of transition metal centers from valence-to-core X-ray emission spectroscopy. *Acc Chem Res* **48**, 2967-2975, doi:10.1021/acs.accounts.5b00309 (2015).

81 Katayama, T. *et al.* A versatile experimental system for tracking ultrafast chemical reactions with X-ray free-electron lasers. *Struct Dyn* **6**, 054302, doi:10.1063/1.5111795 (2019).

82 Ledbetter, K. *et al.* Excited state charge distribution and bond expansion of ferrous complexes observed with femtosecond valence-to-core x-ray emission spectroscopy. *J Chem Phys* **152**, 074203, doi:10.1063/1.5139441 (2020).

83 Katayama, T. *et al.* Femtosecond x-ray absorption spectroscopy with hard x-ray free electron laser. *Appl Phys Lett* **103**, 131105, doi:Artn 131105
10.1063/1.4821108 (2013).

84 Lemke, H. T. *et al.* Femtosecond X-ray absorption spectroscopy at a hard X-ray free electron laser: application to spin crossover dynamics. *J Phys Chem A* **117**, 735-740, doi:10.1021/jp312559h (2013).

85 Levantino, M. *et al.* Observing heme doming in myoglobin with femtosecond X-ray absorption spectroscopy. *Struct Dyn* **2**, 041713, doi:10.1063/1.4921907 (2015).

86 Barends, T. R. *et al.* Direct observation of ultrafast collective motions in CO myoglobin upon ligand dissociation. *Science* **350**, 445-450, doi:10.1126/science.aac5492 (2015).

87 Wernet, P. Chemical interactions and dynamics with femtosecond X-ray spectroscopy and the role of X-ray free-electron lasers. *Philos Trans A Math Phys Eng Sci* **377**, 20170464, doi:10.1098/rsta.2017.0464 (2019).

88 Katayama, T. *et al.* Tracking multiple components of a nuclear wavepacket in photoexcited Cu(I)-phenanthroline complex using ultrafast X-ray spectroscopy. *Nat Commun* **10**, 3606, doi:10.1038/s41467-019-11499-w (2019).

89 Shelby, M. L. *et al.* Ultrafast Excited State Relaxation of a Metalloporphyrin Revealed by Femtosecond X-ray Absorption Spectroscopy. *J Am Chem Soc* **138**, 8752-8764, doi:10.1021/jacs.6b02176 (2016).

90 Miller, N. A. *et al.* Polarized XANES Monitors Femtosecond Structural Evolution of Photoexcited Vitamin B12. *J Am Chem Soc* **139**, 1894-1899, doi:10.1021/jacs.6b11295 (2017).

91 Miller, N. A. *et al.* Ultrafast XANES Monitors Femtosecond Sequential Structural Evolution in Photoexcited Coenzyme B12. *J Phys Chem B* **124**, 199-209, doi:10.1021/acs.jpcb.9b09286 (2020).

92 Chatterjee, R. *et al.* XANES and EXAFS of dilute solutions of transition metals at XFELs. *J Synchrotron Radiat* **26**, 1716-1724, doi:10.1107/S1600577519007550 (2019).

93 Britz, A. *et al.* Resolving structures of transition metal complex reaction intermediates with femtosecond EXAFS. *Phys Chem Chem Phys* **22**, 2660, doi:10.1039/c9cp03483h (2020).

94 Gul, S. *et al.* Simultaneous detection of electronic structure changes from two elements of a bifunctional catalyst using wavelength-dispersive X-ray emission spectroscopy and in situ electrochemistry. *Phys Chem Chem Phys* **17**, 8901-8912, doi:10.1039/c5cp01023c (2015).

95 Alonso-Mori, R. *et al.* Towards characterization of photo-excited electron transfer and catalysis in natural and artificial systems using XFELs. *Faraday Discuss* **194**, 621-638, doi:10.1039/c6fd00084c (2016).

96 Martinie, R. J. *et al.* Two-Color Valence-to-Core X-ray Emission Spectroscopy Tracks Cofactor Protonation State in a Class I Ribonucleotide Reductase. *Angew Chem Int Ed Engl* **57**, 12754-12758, doi:10.1002/anie.201807366 (2018).

97 Canton, S. E. *et al.* Visualizing the non-equilibrium dynamics of photoinduced intramolecular electron transfer with femtosecond X-ray pulses. *Nat Commun* **6**, 6359, doi:10.1038/ncomms7359 (2015).

98 Kern, J. *et al.* Taking snapshots of photosynthetic water oxidation using femtosecond X-ray diffraction and spectroscopy. *Nat Commun* **5**, 4371, doi:10.1038/ncomms5371 (2014).

99 Kupitz, C. *et al.* Serial time-resolved crystallography of photosystem II using a femtosecond X-ray laser. *Nature* **513**, 261-265, doi:10.1038/nature13453 (2014).

100 Suga, M. *et al.* Native structure of photosystem II at 1.95 Å resolution viewed by femtosecond X-ray pulses. *Nature* **517**, 99-103, doi:10.1038/nature13991 (2015).

101 Young, I. D. *et al.* Structure of photosystem II and substrate binding at room temperature. *Nature* **540**, 453-457, doi:10.1038/nature20161 (2016).

102 Suga, M. *et al.* Light-induced structural changes and the site of O=O bond formation in PSII caught by XFEL. *Nature* **543**, 131-135, doi:10.1038/nature21400 (2017).

103 Suga, M. *et al.* An oxyl/oxo mechanism for oxygen-oxygen coupling in PSII revealed by an x-ray free-electron laser. *Science* **366**, 334-338, doi:10.1126/science.aax6998 (2019).

104 Yano, J. *et al.* X-ray Damage to the Mn_4Ca Complex in Photosystem II Crystals: A Case Study for Metallo-Protein X-ray Crystallography. *Proc. Natl. Acad. Sci. USA* **102**, 12047-12052 (2005).

105 Kunnus, K. *et al.* Viewing the Valence Electronic Structure of Ferric and Ferrous Hexacyanide in Solution from the Fe and Cyanide Perspectives. *J Phys Chem B* **120**, 7182-7194, doi:10.1021/acs.jpcb.6b04751 (2016).

106 Dell'Angela, M. *et al.* Real-time observation of surface bond breaking with an x-ray laser. *Science* **339**, 1302-1305, doi:10.1126/science.1231711 (2013).

107 Östrom, H. *et al.* Surface chemistry. Probing the transition state region in catalytic CO oxidation on Ru. *Science* **347**, 978-982, doi:10.1126/science.1261747 (2015).

108 Nilsson, A. *et al.* Catalysis in real time using X-ray lasers. *Chem Phys Lett* **675**, 145-173, doi:10.1016/j.cplett.2017.02.018 (2017).

109 Ismail, A. S. M. *et al.* Direct observation of the electronic states of photoexcited hematite with ultrafast 2p3d X-ray absorption spectroscopy and resonant inelastic X-ray scattering. *Phys Chem Chem Phys* **22**, 2685-2692, doi:10.1039/c9cp03374b (2020).

110 Siefermann, K. R. *et al.* Atomic-Scale Perspective of Ultrafast Charge Transfer at a Dye-Semiconductor Interface. *J. Phys. Chem. Letts.* **5**, 2753-2759, doi:10.1021/jz501264x (2014).

111 Eckert, S. *et al.* Ultrafast Independent N-H and N-C Bond Deformation Investigated with Resonant Inelastic X-Ray Scattering. *Angew Chem Int Ed Engl* **56**, 6088-6092, doi:10.1002/anie.201700239 (2017).

112 Loh, Z. H. *et al.* Observation of the fastest chemical processes in the radiolysis of water. *Science* **367**, 179-182, doi:10.1126/science.aaz4740 (2020).

113 Wolf, T. J. A. *et al.* Probing ultrafast pipi*/npi* internal conversion in organic chromophores via K-edge resonant absorption. *Nat Commun* **8**, 29, doi:10.1038/s41467-017-00069-7 (2017).

114 Wolf, T. J. A. & Guhr, M. Photochemical pathways in nucleobases measured with an X-ray FEL. *Philos Trans A Math Phys Eng Sci* **377**, 20170473, doi:10.1098/rsta.2017.0473 (2019).

115 Gessner, O. & Guhr, M. Monitoring Ultrafast Chemical Dynamics by Time-Domain X-ray Photo- and Auger-Electron Spectroscopy. *Acc Chem Res* **49**, 138-145, doi:10.1021/acs.accounts.5b00361 (2016).

116 Kubin, M. *et al.* Probing the oxidation state of transition metal complexes: a case study on how charge and spin densities determine Mn L-edge X-ray absorption energies. *Chemical Science* **9**, 6813-6829, doi:10.1039/c8sc00550h (2018).

117 Blomberg, M. R. & Siegbahn, P. E. M. A comparative study of high-spin manganese and iron complexes. *Theor Chem Acta* **97**, 72-80 (1997).

118 Lundberg, M. & Delcey, M. G. in *Transition Metals in Coordination Environments: Computational Chemistry and Catalysis Viewpoints* (eds Ewa Broclawik, Tomasz Borowski, & Mariusz Radoń) 185-217 (Springer International Publishing, 2019).

119 Wernet, P. *et al.* Orbital-specific mapping of the ligand exchange dynamics of Fe(CO)5 in solution. *Nature* **520**, 78-81, doi:10.1038/nature14296 (2015).

120 Kunnus, K. *et al.* Identification of the dominant photochemical pathways and mechanistic insights to the ultrafast ligand exchange of $Fe(CO)_5$ to $Fe(CO)_4EtOH$. *Struct Dyn* **3**, 043204, doi:10.1063/1.4941602 (2016).

121 Lundberg, M. & Wernet, P. in *Synchrotron Light Sources and Free-Electron Lasers, 2nd edition* (eds E. J. Jaeschke, S. Khan, J. R. Schneider, & J. B. Hastings) 1-52 (Springer Nature, 2019).

122 Hocking, R. K. *et al.* Fe L-edge XAS studies of $K_4[Fe(CN)_6]$ and $K_3[Fe(CN)_6]$: A direct probe of back-bonding. *Journal of the American Chemical Society* **128**, 10442-10451, doi:10.1021/ja061802i (2006).

123 Jay, R. M. *et al.* Disentangling Transient Charge Density and Metal-Ligand Covalency in Photoexcited Ferricyanide with Femtosecond Resonant Inelastic Soft X-ray Scattering. *J. Phys. Chem. Letts.* **9**, 3538-3543, doi:10.1021/acs.jpclett.8b01429 (2018).

124 Norell, J. *et al.* Fingerprints of electronic, spin and structural dynamics from resonant inelastic soft X-ray scattering in transient photo-chemical species. *Phys Chem Chem Phys* **20**, 7243-7253, doi:10.1039/c7cp08326b (2018).

125 Kunnus, K. *et al.* Chemical control of competing electron transfer pathways in iron tetracyano-polypyridyl photosensitizers. *Chemical Science* **11**, 4360-4373, doi:10.1039/c9sc06272f (2020).

126 Glover, T. E. *et al.* X-ray and optical wave mixing. *Nature* **488**, 603-608, doi:http://www.nature.com/nature/journal/v488/n7413/abs/nature11340.html#supplementary-information (2012).

127 Fuchs, M. *et al.* Anomalous nonlinear X-ray Compton scattering. *Nat Phys* **11**, 964-970, doi:10.1038/nphys3452
http://www.nature.com/nphys/journal/v11/n11/abs/nphys3452.html#supplementary-information (2015).

128 Stöhr, J. Two-Photon X-Ray Diffraction. *Physical Review Letters* **118**, 024801 (2017).

129 Tamasaku, K. *et al.* Nonlinear Spectroscopy with X-Ray Two-Photon Absorption in Metallic Copper. *Physical Review Letters* **121**, 083901, doi:10.1103/PhysRevLett.121.083901 (2018).

130 Shwartz, S. *et al.* X-Ray Second Harmonic Generation. *Physical Review Letters* **112**, 163901, doi:10.1103/PhysRevLett.112.163901 (2014).

131 Foglia, L. *et al.* First Evidence of Purely Extreme-Ultraviolet Four-Wave Mixing. *Physical Review Letters* **120**, 263901, doi:10.1103/PhysRevLett.120.263901 (2018).

132 Bencivenga, F. *et al.* Nanoscale transient gratings excited and probed by extreme ultraviolet femtosecond pulses. *Science Advances* **5**, eaaw5805, doi:10.1126/sciadv.aaw5805 (2019).

133 Svetina, C. *et al.* Towards X-ray transient grating spectroscopy. *Opt. Lett.* **44**, 574-577, doi:10.1364/OL.44.000574 (2019).

134 Rohringer, N. *et al.* Atomic inner-shell X-ray laser at 1.46 nanometres pumped by an X-ray free-electron laser. *Nature* **481**, 488-491, doi:10.1038/nature10721 (2012).

135 Weninger, C. *et al.* Stimulated electronic x-ray Raman scattering. *Phys Rev Lett* **111**, 233902, doi:10.1103/PhysRevLett.111.233902 (2013).

136 Yoneda, H. *et al.* Atomic inner-shell laser at 1.5-angstrom wavelength pumped by an X-ray free-electron laser. *Nature* **524**, 446-449, doi:10.1038/nature14894 (2015).

137 Kroll, T. *et al.* Stimulated X-ray emission spectroscopy in transition metal complexes. *Phys Rev Lett* **120**, 133203, doi:10.1103/PhysRevLett.120.133203 (2018).

138 Kroll, T. *et al.* Observation of Seeded Mn Kβ Stimulated X-Ray Emission Using Two-Color X-Ray Free-Electron Laser Pulses. *Physical Review Letters* **125**, doi:10.1103/PhysRevLett.125.037404 (2020).

139 Cederbaum, L. S., Tarantelli, F., Sgamellotti, A. & Schirmer, J. On double vacancies in the core. *The Journal of Chemical Physics* **85**, 6513-6523, doi:10.1063/1.451432 (1986).

140 Ågren, H. & Jensen, H. J. A. Relaxation and correlation contributions to molecular double core ionization energies. *Chem Phys* **172**, 45-57, doi:10.1016/0301-0104(93)80105-i (1993).

141 Tashiro, M., Ueda, K. & Ehara, M. Double core–hole correlation satellite spectra of N_2 and CO molecules. *Chem Phys Lett* **521**, 45-51, doi:10.1016/j.cplett.2011.11.062 (2012).

142 Thomas, T. D. Single and double core-hole ionization energies in molecules. *J Phys Chem A* **116**, 3856-3865, doi:10.1021/jp211741e (2012).

143 Takahashi, O. & Ueda, K. Molecular double core-hole electron spectroscopy for probing chemical bonds: C60 and chain molecules revisited. *Chem Phys* **440**, 64-68, doi:10.1016/j.chemphys.2014.06.007 (2014).

144 Koulentianos, D. *et al.* KL double core hole pre-edge states of HCl. *Phys Chem Chem Phys* **20**, 2724-2730, doi:10.1039/c7cp04214k (2018).

145 Linusson, P., Takahashi, O., Ueda, K., Eland, J. H. D. & Feifel, R. Structure sensitivity of double inner-shell holes in sulfur-containing molecules. *Phys Rev A* **83**, 022506, doi:10.1103/PhysRevA.83.022506 (2011).

146 Lablanquie, P. *et al.* Evidence of single-photon two-site core double ionization of C2H2 molecules. *Phys Rev Lett* **107**, 193004, doi:10.1103/PhysRevLett.107.193004 (2011).

147 Tashiro, M. *et al.* Auger decay of molecular double core-hole and its satellite states: comparison of experiment and calculation. *J Chem Phys* **137**, 224306, doi:10.1063/1.4769777 (2012).

148 Nakano, M. *et al.* Single photon K(-2) and K(-1)K(-1) double core ionization in C_2H_{2n} (n=1-3), CO, and N_2 as a potential new tool for chemical analysis. *Phys Rev Lett* **110**, 163001, doi:10.1103/PhysRevLett.110.163001 (2013).

149 Carniato, S. *et al.* Single photon simultaneous K-shell ionization and K-shell excitation. I. Theoretical model applied to the interpretation of experimental results on H_2O. *J Chem Phys* **142**, 014307, doi:10.1063/1.4904273 (2015).

150 Penent, F. *et al.* Double core hole spectroscopy with synchrotron radiation. *J Elec Spect Rel Phen* **204**, 303-312, doi:10.1016/j.elspec.2015.06.015 (2015).

151 Young, L. *et al.* Femtosecond electronic response of atoms to ultra-intense X-rays. *Nature* **466**, 56-56, doi:10.1038/nature09177 (2010).

152 Cryan, J. P. *et al.* Auger Electron Angular Distribution of Double Core-Hole States in the Molecular Reference Frame. *Physical Review Letters* **105**, 083004, doi:10.1103/PhysRevLett.105.083004 (2010).

153 Fang, L. *et al.* Double Core-Hole Production in N_2: Beating the Auger Clock. *Physical Review Letters* **105**, 083005, doi:10.1103/PhysRevLett.105.083005 (2010).

154 Salen, P. *et al.* Experimental verification of the chemical sensitivity of two-site double core-hole states formed by an x-ray free-electron laser. *Phys Rev Lett* **108**, 153003, doi:10.1103/PhysRevLett.108.153003 (2012).

155 Piancastelli, M. N. K-shell double core-hole spectroscopy in molecules. *Eur Phys J Special Topics* **222**, 2035-2055, doi:10.1140/epjst/e2013-01985-9 (2013).

156 Zhaunerchyk, V. *et al.* Disentangling formation of multiple-core holes in aminophenol molecules exposed to bright X-FEL radiation. *J Phys B: Atom Mol Optical Phys* **48**, doi:10.1088/0953-4075/48/24/244003 (2015).

157 Zhang, Y., Bergmann, U., Schoenlein, R., Khalil, M. & Govind, N. Double core hole valence-to-core x-ray emission spectroscopy: A theoretical exploration using time-dependent density functional theory. *J Chem Phys* **151**, 144114, doi:10.1063/1.5111141 (2019).

158 Hua, W., Bennett, K., Zhang, Y., Luo, Y. & Mukamel, S. Study of double core hole excitations in molecules by X-ray double-quantum-coherence signals: a multi-configuration simulation. *Chem Sci* **7**, 5922-5933, doi:10.1039/c6sc01571a (2016).

159 Mukamel, S. *et al.* Coherent multidimensional optical probes for electron correlations and exciton dynamics: from NMR to X-rays. *Acc Chem Res* **42**, 553-562, doi:10.1021/ar800258z (2009).

160 Schweigert, I. V. & Mukamel, S. Coherent ultrafast core-hole correlation spectroscopy: x-ray analogues of multidimensional NMR. *Phys Rev Lett* **99**, 163001, doi:10.1103/PhysRevLett.99.163001 (2007).

161 Li, X., Zhang, T., Borca, C. N. & Cundiff, S. T. Many-body interactions in semiconductors probed by optical two-dimensional fourier transform spectroscopy. *Phys Rev Lett* **96**, 057406, doi:10.1103/PhysRevLett.96.057406 (2006).

162 Brixner, T. *et al.* Two-dimensional spectroscopy of electronic couplings in photosynthesis. *Nature* **434**, 625-628, doi:10.1038/nature03429 (2005).

163 Tanaka, S. & Mukamel, S. Coherent x-ray Raman spectroscopy: a nonlinear local probe for electronic excitations. *Phys Rev Lett* **89**, 043001, doi:10.1103/PhysRevLett.89.043001 (2002).

164 Bergmann, U., Yachandra, V. K. & Yano, J. (Royal Society of Chemistry, London, UK, 2017).

165 Jaeschke, E. J., Khan, S., Schneider, J. R. & Hastings, J. B. (Springer Nature, 2016).

166 Agarwal, P. K. *X-Ray Spectroscopy An Introduction*. (Springer, 1991).

167 Henke, B. L., Gullikson, E. M. & Davis, J. C. X-Ray Interactions - Photoabsorption, Scattering, Transmission, and Reflection at E=50-30,000 Ev, Z=1-92. *Atom Data Nucl Data* **54**, 181-342, doi:10.1006/adnd.1993.1013 (1993).

168 Siegbahn, K. *ESCA applied to free molecules*. (North-Holland Publishers, 1969).

169 Gelius, U. Binding Energies and Chemical Shifts in ESCA. *Phys Scripta* **9**, 133-147, doi:10.1088/0031-8949/9/3/001 (1974).

170 Stöhr, J. *NEXAFS Spectroscopy*. (Springer Berlin Heidelberg, 2013).

171 de Groot, F. M. F. Ligand and metal X-ray absorption in transition metal complexes. *Inorg Chim Acta* **361**, 850-856 (2008).

172 Koningsberger, D. C. & Prins, R. Vol. 92 *Chemical Analysis* (John Wiley & Sons, New York, 1988).

173 de Groot, F. M. F. Multiplet effects in X-ray spectroscopy. *Coord Chem Rev* **249**, 31-63 (2005).

174 de Groot, F. M. F. X-ray absorption and dichroism of transition metals and their compounds. *J. Electron Spectrosc. Relat. Phenom.* **67**, 529-622 (1994).

175 Stern, E. A. Musings about the development of XAFS. *J Synchrotron Radiat* **8**, 49-54, doi:Doi 10.1107/S0909049500014138 (2001).

176 Meisel, A., Leonhardt, G. & Szargan, R. *X-Ray Spectra and Chemical Binding*. (Springer, 1989).

177 Kotani, A. & Shin, S. Resonant inelastic x-ray scattering spectra for electrons in solids. *Reviews of Modern Physics* **73**, 203-246, doi:DOI 10.1103/RevModPhys.73.203 (2001).

178 de Groot, F. & Kotani, A. *Core Level Spectoscopy of Solids*. (CRC Press, 2008).

179 Hahn, A. W. *et al.* Probing the Valence Electronic Structure of Low-Spin Ferrous and Ferric Complexes Using 2p3d Resonant Inelastic X-ray Scattering (RIXS). *Inorg Chem* **57**, 9515-9530, doi:10.1021/acs.inorgchem.8b01550 (2018).

180 Van Kuiken, B. E., Hahn, A. W., Maganas, D. & DeBeer, S. Measuring Spin-Allowed and Spin-Forbidden d-d Excitations in Vanadium Complexes with 2p3d Resonant Inelastic X-ray Scattering. *Inorg. Chem.* **55**, 11497-11501, doi:10.1021/acs.inorgchem.6b02053 (2016).

181 Mitzner, R. *et al.* L-edge X-ray absorption spectroscopy of dilute systems relevant to metalloproteins using an X-ray free-electron laser. *J. Phys. Chem. Letts.* **4**, 3641-3647, doi:10.1021/jz401837f (2013).

182 Bergmann, U. & Glatzel, P. X-ray emission spectroscopy. *Photosynth Res* **102**, 255-266, doi:10.1007/s11120-009-9483-6 (2009).

183 Schoenlein, R. *et al.* Recent advances in ultrafast X-ray sources. *Philosophical Transactions of the Royal Society A: Mathematical, Physical and Engineering Sciences* **377**, 20180384, doi:doi:10.1098/rsta.2018.0384 (2019).